Radar Signatures and Surface Observations of Elevated Convection Associated with Damaging Surface Winds

BRETT S. BORCHARDT,[a] KEITH D. SHERBURN,[b] AND RUSS S. SCHUMACHER[c]

[a] *NOAA/National Weather Service, Romeoville, Illinois*
[b] *NOAA/National Weather Service, Rapid City, South Dakota*
[c] *Department of Atmospheric Science, Colorado State University, Fort Collins, Colorado*

(Manuscript received 6 October 2023, in final form 16 December 2023, accepted 6 February 2024)

ABSTRACT: Identifying radar signatures indicative of damaging surface winds produced by convection remains a challenge for operational meteorologists, especially within environments characterized by strong low-level static stability and convection for which inflow is presumably entirely above the planetary boundary layer. Numerical model simulations suggest the most prevalent method through which elevated convection generates damaging surface winds is via "up–down" trajectories, where a near-surface stable layer is dynamically lifted and then dropped with little to no connection to momentum associated with the elevated convection itself. Recently, a number of unique convective episodes during which damaging surface winds were produced by apparently elevated convection coincident with mesoscale gravity waves were identified and cataloged for study. A novel radar signature indicative of damaging surface winds produced by elevated convection is introduced through six representative cases. One case is then explored further via a high-resolution model simulation and related to the conceptual model of up–down trajectories. Understanding the processes responsible for, and radar signature indicative of, damaging surface winds produced by gravity wave coincident convection will help operational forecasters identify and ultimately warn for a previously underappreciated phenomenon that poses a threat to lives and property.

SIGNIFICANCE STATEMENT: We identified unique radar and observational signatures of thunderstorms that produce damaging surface winds through a recently discovered mechanism. The radar and observational signatures can be used to issue warnings to protect lives and property in situations where damaging winds were previously unexpected. Key observational signatures include associated increases in surface pressure, sustained wind, and wind gust magnitudes, as well as little to no change or an increase in surface temperature. In addition, base radar data exhibit a divergence signature, including in regions of little or no detectable precipitation. Additional study is needed to answer why some atmospheric environments are supportive of the unique damaging-wind-producing mechanism while others are not.

KEYWORDS: Downbursts; Severe storms; Wind; Convective storms; Small scale processes; Radars/Radar observations

1. Introduction

Severe convection[1] is defined as any convective cell or complex that produces a tornado, surface[2] wind gusts of at least 25.7 m s^{-1} (50 kt, where 1 kt ≈ 0.51 m s^{-1}; 58 mph), or hail at least 2.54 cm (1 in.) in diameter. All modes of convection (e.g., supercell, multicell, and single cell) are capable of producing damaging surface winds across the country throughout the year (Smith et al. 2013). Considering that damaging convective wind events can be just as impactful as tornadoes and hurricanes in terms of property damage, injuries, and fatalities (e.g., Ashley and Mote 2005), a number of strategies have been developed to identify and warn for such events including, but not limited to, identifying favorable environments (e.g., Kuchera and Parker 2006); leveraging radar structures such as bow echoes, the rear-inflow notch, areas of midaltitude radial convergence (MARC), and mesovortices (Przybylinski 1995; Schmocker et al. 1996; Weisman and Trapp 2003; Wakimoto et al. 2006; Atkins and St. Laurent 2009); prognostic tools such as the wind gust ratio (Sherburn et al. 2021); and image processing of radar imagery (Ibrahim et al. 2023). Even with knowledge of environments and radar signatures favorable for damaging surface winds, missed events continue.

Convection can be broken into two general categories: surface-based and elevated. Compared to surface-based convection, where updraft inflow includes unstable air from close to the ground, elevated convection is supported by unstable air that originates above a surface-based statically stable layer (e.g., Colman 1990; Parker 2008). Elevated convection can adopt the same structures and storm modes as surface-based counterparts, including supercells, mesoscale convective complexes and systems, and single cells.

In a 5-yr climatology of elevated severe convective storms in the United States, Horgan et al. (2007) found that the most

[1] The term "convection" will refer to deep moist convection unless otherwise stated.
[2] The term "surface" refers to observed wind at a 10-m height, the standard height of an anemometer on most operational observing systems.

Corresponding author: Brett S. Borchardt, brett.borchardt@noaa.gov

DOI: 10.1175/WAF-D-23-0171.1

© 2024 American Meteorological Society. This published article is licensed under the terms of the default AMS reuse license. For information regarding reuse of this content and general copyright information, consult the AMS Copyright Policy (www.ametsoc.org/PUBSReuseLicenses).

Brought to you by NOAA Central Library | Unauthenticated | Downloaded 08/28/24 03:27 PM UTC

common severe storm report was severe hail (59%), followed by damaging surface winds (37%) and tornadoes (4%). Similar statistics were found in a 20-yr climatology of nocturnal warm-season convection conducted by Reif and Bluestein (2017), wherein 80% of nocturnal damaging wind events were initiated along or on the cold side of surface boundaries. While the mechanisms for damaging wind production in surface-based systems—such as precipitation loading and downdrafts (e.g., Wakimoto 2001), rear-inflow jets (e.g., Smull and Houze 1987; Weisman 1993), and mesovortices (e.g., Weisman and Trapp 2003; Atkins et al. 2005; Wakimoto et al. 2006)—are generally well understood, the mechanisms responsible for damaging surface winds in elevated convection are less clear. Indeed, the presence of a surface stable layer through which downward momentum cannot penetrate (e.g., akin to the "cushion stage"; Fujita 1981) has long been thought to be the reason for a lower frequency of damaging winds than severe hail with elevated convection (e.g., Proctor 1989; Horgan et al. 2007; Marsham et al. 2010; Reif and Bluestein 2017).

Many, if not all, of the few well-documented cases of elevated convection producing damaging surface winds appear to be related to up–down trajectories wherein a near-surface stable layer is first lifted upward via vertical dynamic perturbation pressure gradient accelerations or wave dynamics (i.e., not buoyancy) and then pushed rapidly downward due to negative buoyancy, condensate loading, or separate near-surface perturbation pressure gradient accelerations (Knupp 1996; Schmidt and Cotton 1989). For example, Bernardet and Cotton (1998) and MacIntosh and Parker (2017) identified up–down trajectories forced by vertical accelerations owing to perturbation pressure gradients within rotating updrafts as a cause for damaging surface winds in simulations of elevated convection. Schumacher et al. (2023; hereinafter S23) identified updrafts and downdrafts associated with internal mesoscale gravity waves (MGWs) coincident with multiple bands of elevated convection as another way to generate up–down trajectories and hence damaging surface winds, similar to the process that causes a downslope windstorm (e.g., Peltier and Clark 1979). The elevated supercell studied in MacIntosh and Parker (2017) was the leading convective cell in an MGW packet (not shown), suggesting both gravity waves and perturbation vorticity within an updraft may generate up–down trajectories in tandem or at least within similar environments.[3]

MGWs are ubiquitous in the atmosphere and are defined by buoyancy oscillations within a ducted neutrally or unstably stratified layer with frequencies based on the Brunt–Väisälä frequency. Generally speaking, MGW events can occur during any time of year, with the highest frequency during the late winter to early summer (Koppel et al. 2000). MGWs can develop through a spontaneous balance adjustment to upper-level flow in response to the displacement of thermally direct ageostrophic circulations offset from the exit region of curved jet streaks, especially among rapidly strengthening baroclinic systems (i.e., very strong synoptic-scale forcing; Uccellini and Koch 1987; Zhang et al. 2001). The generation of MGWs can also result from the lifting of a surface-based stable layer by a gravity current including a convective cold pool (e.g., Fulton et al. 1990; Knupp 2006; Toms et al. 2017), topography (e.g., Zhang and Koch 2000; Ruppert and Bosart 2014), or front (e.g., Koch and Clark 1999) via the propagation of semipermanent upward displacements of the surface layer (i.e., a bore; Tepper 1950; Clarke et al. 1981; Mahapatra et al. 1991) or oscillations of the surface stable layer itself (a soliton; e.g., Christie et al. 1978; Doviak and Ge 1984). Common mechanisms to generate MGWs are shown for reference in Fig. 1.

Convection and MGWs are inevitably interlinked. In addition to the generation of bores and solitons through the lifting of a surface stable layer by a convective gravity current, latent heating within updraft towers of convection can generate MGWs (e.g., Powers and Reed 1993; Fovell et al. 2006; S23). All the same, MGWs of both convective and nonconvective origins can also initiate convective updrafts (e.g., Uccelini 1975; Koch et al. 1988; Rottman et al. 1992; Knupp 2006; Parsons et al. 2019) and may even serve as an important mechanism to maintain elevated convection (e.g., Parker 2008; French and Parker 2010; Marsham et al. 2011; Blake et al. 2017; Du and Zhang 2019). Gravity waves and convection can behave in a synergistic relationship through a process known as ducted-wave convection instability of the second kind (ducted-wave CISK; Zhang et al. 2001). Theoretically, convection initiated by MGWs can also produce its own MGWs, leading to complex interactions. For a more in-depth and eloquent review of the role of moist convection on the development and maintenance of MGWs, refer to Ruppert et al. (2022).

Turbulent MGWs are often accompanied by jumps in surface pressure, sustained winds, and wind gusts, with corresponding shifts in wind direction toward the direction of wave propagation (e.g., Knupp 2006; Marsham et al. 2010; Toms et al. 2017; Parsons et al. 2019; Anderson and Mann 2020). Unlike with gravity currents, which are associated with falling temperatures due to the horizontal advection of cool, dense air, turbulent MGWs are often accompanied by either steady or modestly warming surface temperatures owing to the downward mixing of drier and warmer air above a surface inversion (Clarke et al. 1981; Mahapatra et al. 1991; Koppel et al. 2000; Koch et al. 2008). As a result, steady or rising surface temperatures are often a helpful discriminator between gravity currents and turbulent waves, which are otherwise accompanied by correlated increases in wind magnitude and pressure.

Owing to the presumed limited frequency of damaging surface winds produced by elevated convection and a limited number of studies investigating the methods by which they may occur, there are few, if any, operational methods to forecast or identify upcoming or ongoing events. Moreover, it appears that the momentum of downdrafts produced by the convection itself may not be completely responsible for damaging surface winds produced by elevated convection—contrary to the typical source of damaging winds from

[3] MGWs have also been implicated in the production of damaging surface winds within stabilized air masses behind mature convective systems (surface-based or elevated) owing to perturbation pressure gradient accelerations related to mesohigh–wake low couplets (e.g., Coleman and Knupp 2009; Ruppert and Bosart 2014). Such a process is not the focus of this study.

Brought to you by NOAA Central Library | Unauthenticated | Downloaded 08/28/24 03:27 PM UTC

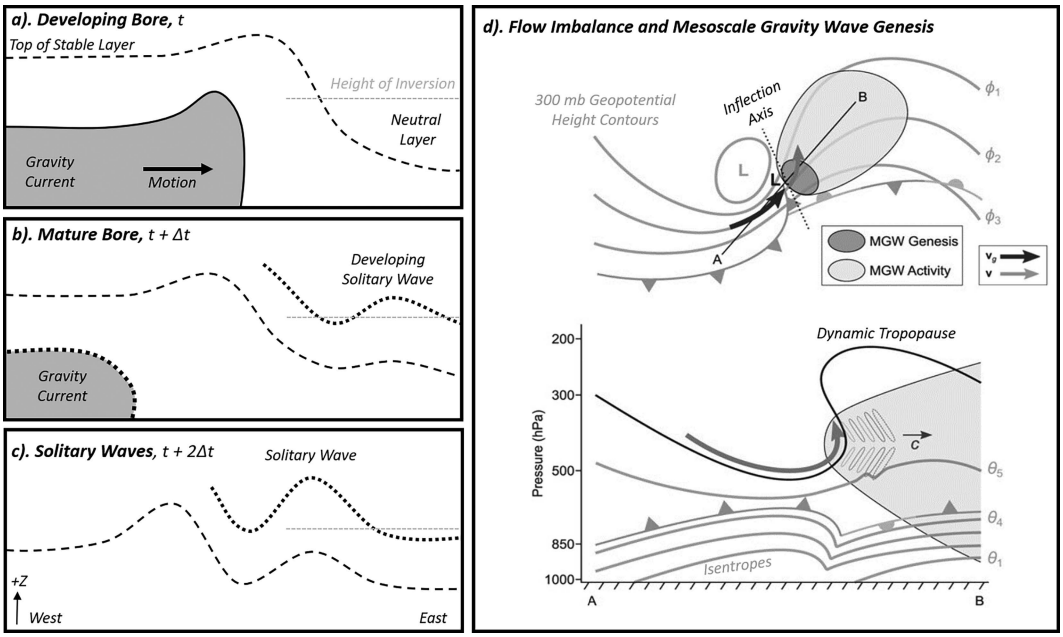

FIG. 1. Based on Fig. 1 of Knupp (2006), the general evolution as viewed by a vertical cross section from (a) a developing bore to (b) a mature bore and (c) solitary wave within an environment characterized by a neutral layer bounded by an inversion and surface stable layer as labeled in the figure; (d) part of Fig. 5 from Ruppert et al. (2022) showing a conceptual model of favorable environment supportive of the genesis of MGWs. The top of (d) shows the 300-mb geopotential height (gray contours), total and geostrophic wind (gray and black arrows, respectively), surface and upper-level cyclones (black and gray "L" letters, respectively), and inflection axis (dotted black line). The bottom of (d) shows a cross section through the line "A–B" as shown in the top panel with isentropes (gray contours), total flow (gray arrow), and the dynamic tropopause (black contour). Fronts with conventional symbology are shown in both the top and bottom of (d). © American Meteorological Society. Used with permission.

surface-based convection. For these reasons, damaging surface winds produced by elevated convection may catch forecasters and the public by surprise, posing an important operational challenge. Ironically, the same is true for forecasting and identifying MGW events in spite of their common frequency and wealth of historical and recent literature on their development, maintenance, and ultimate cause of hazardous meteorological phenomena beyond convection (e.g., Ruppert et al. 2022). In a moment of perhaps unanticipated prescience, Koch and Saleeby (2001) noted the following:

> "Despite the significant impact that gravity waves can impose upon weather conditions and their common occurrence, these phenomena are rarely considered in preparation of NWS forecast discussions. The forecaster is largely concerned with meteorological phenomena that are better understood and more easily detected and examined through satellite and radar imagery and numerical model results. For these reasons, gravity waves have remained primarily of research interest and have yet to find their way into daily operational forecasting practices."[4]

For this study, instances of damaging-wind-producing elevated convection in equally spaced bands (indicative of MGWs) located on the cool side of frontal zones were identified and cataloged. In several cases, the winds were significantly damaging, including measured wind gusts of at least 33.4 m s^{-1} (65 kt; Hales 1988),[5] reports of structural damage to buildings, and injuries, confirming the events pose a threat to lives and property. Convection and observations in each case appear to depict qualitatively similar radar signatures, overall convective evolutions, and surface pressure trends during the production of damaging surface winds despite diversity in location, time of day, and/or season. The common radar signature appears to align with the conceptual model of up–down trajectories and, accordingly, appears to be a marker for damaging winds produced by elevated convection associated with MGWs.

By presenting a brief climatology of events, common radar and observational signatures associated with damaging wind production, and a connection with the theoretical idea of up–down trajectories facilitated by MGWs through a brief analysis of a high-resolution model simulation, we will show the following:

1) Contrary to operational wisdom, certain types of elevated convection are capable of producing damaging winds regardless of geographic location, time of day, or time of year.

[4] There are many ways that an NWS forecaster can communicate a forecast for and impacts of MGWs. Regardless, their common omission in NWS forecast discussions implies that they are not regularly forecasted by a large subset of operational meteorologists.

[5] For the sake of clarity and comparison with traditional units used by operational meteorologists when interrogating radar data, all wind measurements hereafter will be in knots (kt).

Brought to you by NOAA Central Library | Unauthenticated | Downloaded 08/28/24 03:27 PM UTC

2) Damaging winds produced by elevated convection are identifiable in real time via consistent radar and observational signatures.

2. Generalized description of cases used in this study

a. Identification and description of cases

The identification of cases during which presumably elevated convection coincident with MGWs produced damaging surface winds was initially based on operational experience. After comparing the initial cases, a consistent radar signature and observational pattern emerged. To test the consistency of the radar and observational patterns between events and provide context to the frequency of what is traditionally considered a rare event, a 2-yr climatology of gravity wave coincident convection was created using the following method:

1) First, national mosaic radar imagery was viewed from the UCAR Mesoscale and Microscale Meteorology (MMM) radar composite archive (http://www2.mmm.ucar.edu/imagearchive/) to identify instances of single or multiple equally spaced arcing bands of convection indicative of MGWs. Events that were entirely or partially outside the boundaries of the contiguous United States were not included.
2) Next, radar data from NWS-maintained Weather Surveillance Radar-1988 Dopplers (WSR-88Ds) were downloaded from the Amazon Cloud Web Services database (https://s3.amazonaws.com/noaa-nexrad-level2/index.html) to confirm convection was indeed equally spaced and propagated in similar directions and speeds for a period of at least 3 h consistent with external forcing (such as an MGW).
3) Finally, convection was confirmed to be elevated by either identifying obvious surface boundaries in radar data (e.g., outflow or frontal boundaries) or by comparing the location of convection with frontal boundaries annotated on archived surface analysis charts cataloged by the Weather Prediction Center (WPC; available at https://www.wpc.ncep.noaa.gov/archives/web_pages/sfc/sfc_archive.php).[6]

If all three conditions were met, the case was cataloged in the climatology.

Each event was then categorized as *damaging, significantly damaging, potentially damaging*, or *nondamaging* using the following scheme:

- If there were reports of wind damage, including estimated or measured wind gusts equal to or greater than 50 kt but less than 65 kt, corresponding to any individual band of convection in NOAA's *Storm Data* publication (StormData), the event was classified as damaging.
- If the reports associated with any band of convection in StormData were cataloged with estimated or measured wind gusts equal to or greater than 65 kt, the event was classified as significantly damaging.
- If there were no reports of wind damage in StormData corresponding to any convective band, but maximum radar base velocity values associated with any feature equaled or exceeded 50 kt for more than three continuous scans, the event was classified as potentially damaging.
- If there were no reports of wind damage in StormData corresponding to any convective band and base velocity values were less than 50 kt through the entirety of the convective episode, the event was classified as nondamaging.

The method was completed for the years 2021 and 2022, leading to the identification of 52 cases, of which 12 were classified as damaging, 5 as potentially damaging, 9 as significantly damaging, and 26 as nondamaging. When combining the damaging, potentially damaging, and significantly damaging cases together (i.e., damaging-wind-producing cases), there were equal parts damaging-wind-producing and nondamaging-wind-producing events within the 2-yr climatology.

It is worth noting that when a measured wind gust is not available, wind damage reports in StormData are well known to be imperfect, with both high and low biases of estimated wind speeds (e.g., Trapp et al. 2006; Edwards et al. 2018). In addition, the absence of a wind report does not necessarily mean that damaging winds did not occur. Confidence in the occurrence of severe weather can be reasonably tied to the number of associated severe weather reports. Of the 21 cases where damaging wind reports were included in StormData, only five were associated with a single report. Of the five cases with a single report of wind damage, four were associated with measured wind gust. As a result, we have confidence that the events classified as damaging were indeed associated with damaging surface winds.

Reports of tornadoes and severe hail were also cataloged for each case to provide context of the frequency of any severe weather produced by convection coincident with MGWs. In total, there were 1094 reports of severe weather, of which 658 (60.1%) were for hail, 433 (40.0%) were for wind, and 3 (approximately 0.2%) were for tornadoes.[7] Of the 52 cases, 26 (50.0%) were associated with only severe hail or severe wind, while 15 (28.8%) were associated with severe winds and hail. Two cases (3.8%) were associated with a report of a tornado. There were 11 events (21.2%) that were associated with hailstones greater than 5.08 cm (2.00 in.) or winds greater

[6] Ideally, data from radiosondes in close proximity to ongoing convection should be examined to assess whether convective inflow is likely to be elevated. However, spatiotemporal limitations in the availability of radiosonde data prevent standardized examinations for all currently known cases. Examining forecast sounding data also presents challenges for analysis owing to a requirement that the simulated environmental data are truly representative of ongoing convection. Hence, while we are confident the convection we identified is elevated, we would be remiss to ignore the possibility that some may have actually been at least partially surface-based.

[7] A report of a tornado is in obvious conflict with an elevated storm mode. A brief analysis of radar data leading up to, during, and after each tornado report in our climatology did not reveal any discernible or persistent low-level rotation. We also note that a finite number of tornado reports were included in the climatology of Horgan et al. (2007).

Brought to you by NOAA Central Library | Unauthenticated | Downloaded 08/28/24 03:27 PM UTC

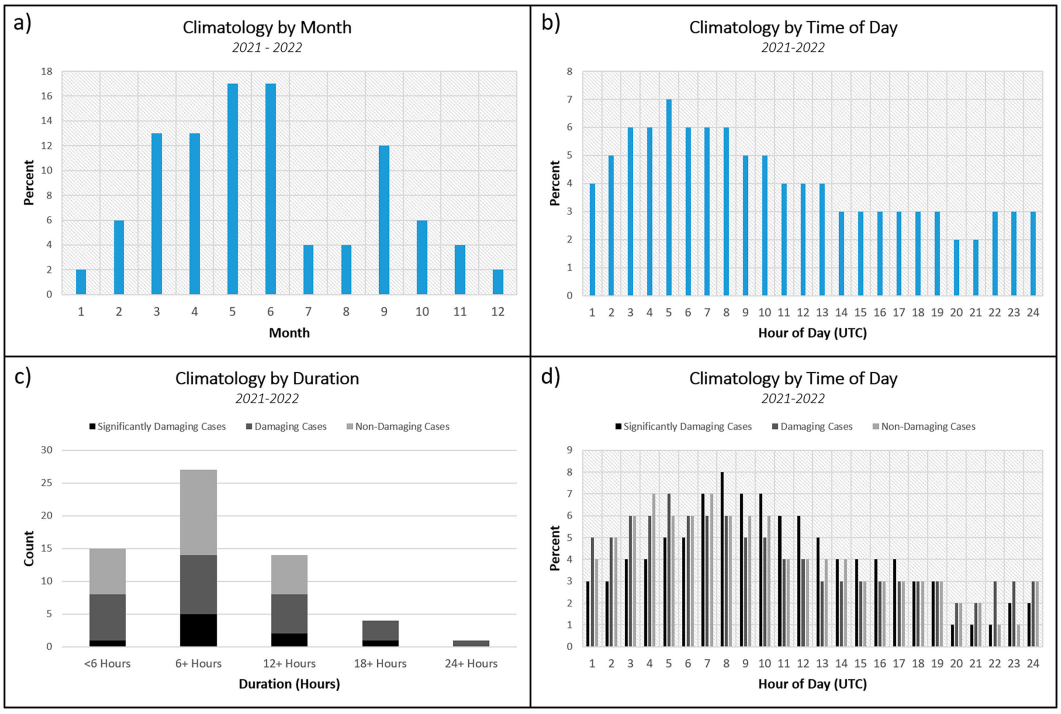

FIG. 2. Normalized frequency of gravity wave coincident convection for the years 2021–22 by (a) month and (b) time of day. (c) The count of damaging, significantly damaging, and nondamaging events by event duration. (d) The normalized frequency of gravity wave coincident convection by time of day and category. The frequency of every hour in (b) and (d) was determined by whether MGW-associated convection was ongoing at that hour within each individual convective episode and not necessarily when severe weather was reported.

than 65 kt. Except for a lower frequency of tornadoes, the report climatology included herein is similar to that for elevated convection reported by Horgan et al. (2007).

From this point forward, "severe" will only refer to damaging-wind-producing convection and "nonsevere" will only refer to nondamaging-wind-producing convection. Moreover, potentially damaging and damaging events will be treated together.[8] A full list of cases, including dates, estimated start and end times, geographic regions, and peak wind gusts and hail sizes within the 2-yr climatology, along with an additional eight cases collected through operational experience, is provided in the appendix.[9]

b. *Case climatology*

Figure 2a shows the normalized frequency of events by time of year and time of day within the 2-yr climatology. Unlike the majority of severe or damaging-wind-producing convection that peaks during the warm season (e.g., April–August; Kelly et al. 1985; Smith et al. 2013), MGW convective events within the 2-yr climatology appear to be most common during the transition months (i.e., spring and fall; Fig. 2a) and may be related to a dependence on the overlap of synoptic-scale forcing for MGWs atop readily available convective instability. Moreover, the monthly climatology of MGW convective events is nearly identical to a 4-yr climatology of elevated convection cataloged by Colman (1990) and the 25-yr climatology of gravity wave events performed by Koppel et al. (2000)—especially those coincident with convection (cf. Fig. 2a with Fig. 9b of Koppel et al. 2000). Accordingly, the relatively short 2-yr climatology presented herein appears to offer a representative snapshot of gravity wave coincident convection as a whole. Considering the frequency of events by category roughly matches that of all events, the time of year does not appear to be not a helpful discriminator between damaging, significantly damaging, and nondamaging events (not shown).

Convective MGW events were most frequent during the nocturnal hours when stable layers are most common owing to the diurnal cooling of the boundary layer, with approximately 66% of all events occurring between 0000 and 1200 UTC (Fig. 2b). The time of day did not appear to be a strong discriminator between severe and nonsevere events (not shown), though significantly damaging events appeared to occur more often during the

[8] While radar base velocity values are dependent on storm motion as well as the orientation to and distance from a sampling radar, the presence of at least three continuous scans with 50-kt velocity returns associated with traditional surface-based storm modes would prompt an NWS forecaster to consider issuing a severe thunderstorm warning. For this reason, as well as known limitations of missing or poor-quality reports in StormData, we will treat "potentially damaging" and "damaging" as the same.

[9] Because the additional eight cases were not collected systematically, they will not be included in section 2b. However, they are included in other sections of our manuscript.

Brought to you by NOAA Central Library | Unauthenticated | Downloaded 08/28/24 03:27 PM UTC

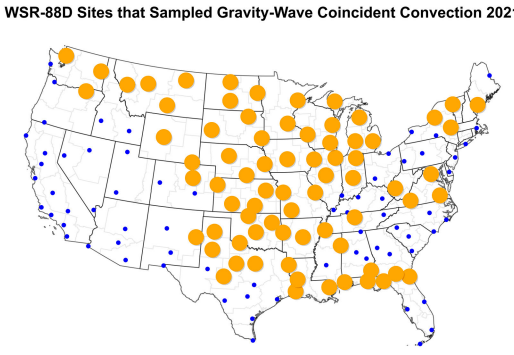

FIG. 3. Locations of WSR-88D radars across the contiguous United States. Orange dots indicate radars that sampled gravity wave coincident convection for the years 2021–22, while blue dots indicate radars that did not sample gravity wave coincident convection.

nighttime, with approximately 66% taking place between 0000 and 1200 UTC and nearly 41% occurring between 0600 and 1200 UTC (Fig. 2d). Accordingly, convective MGW events may be prone to producing significantly damaging winds outside the "traditional" afternoon and evening hours of all significantly damaging wind events (e.g., see Fig. 6 of Kelly et al. 1985). The majority of MGW convective events also lasted between 7 and 12 h, with the shortest duration being just 3 h and the longest nearly 48 h. As shown in Fig. 2c, the majority of events last at least 6 h, with a hint of a signal that severe events lasted longer than nonsevere events, especially considering there were no known nondamaging events that lasted longer than 18 h. A comparatively larger sample size would be helpful to confirm such a finding.

Figure 3 shows the locations of WSR-88D radars that sampled gravity wave coincident convection at least once in the 2-yr climatology. It is readily apparent that gravity wave coincident convection can occur across much of the contiguous United States among a rich diversity in location, ranging from the Pacific Northwest to the Plains, Great Lakes, northeastern United States, and Gulf of Mexico, beyond that originally identified by Koppel et al. (2000). Separating out radars that sampled damaging, nondamaging, and significantly damaging events did not indicate regionality to specific event types except for a lack of severe events in the northeastern United States (not shown). Moreover, the frequency of events regardless of category was similar across the central United States with relatively fewer events observed west of the Rocky Mountains, much in line with a climatology of elevated severe convection in general (e.g., Horgan et al. 2007). Expanding the climatology beyond 2 years would likely uncover additional MGW-coincident convective events, including across the eastern United States in line with observations of nonconvective MGW events (e.g., Zhang et al. 2001).

Among the significantly damaging events within the 2-yr climatology, including those collected through operational experience, a subset was associated with destructive winds with measured or estimated wind gusts well in excess of 65 kt. The strongest measured wind gusts across all known events were 99 kt, first with a destructive macroburst that impacted Akron, Colorado, on 9 June 2020 (Childs et al. 2021; hereinafter C21) and a second time with an apparent supercell during the early morning of 12 March 2021 in southern Kansas. In several cases, structural damage to homes, businesses, and agricultural facilities was common, as were injuries to both animals and humans, underscoring the potential impacts on lives and property associated with these events.

3. Radar signatures and surface observation patterns

Among all cases identified thus far, six were selected for demonstration purposes based on a diversity of geographic location, time of day during which convection occurred, distance from sampling radars, and the proximity of Automated Surface Observing Systems (ASOSs) maintained by the NWS for which observational data can be readily downloaded and examined. Damaging winds were reported or measured in five of the six cases, providing the ability to compare radar signatures and observational patterns between severe and nonsevere events. Table 1 shows the dates on which the convective episodes occurred, the maximum estimated and measured wind gusts produced by the convection, and information pertaining to consistent panels of forthcoming figures to aid in comparison between cases.

As shown in Fig. 4, severe wind reports in each representative case occurred within regions of no or little analyzed surface-based convective available potential energy (SBCAPE), suggesting the responsible convection was elevated. Peak estimated or measured winds in each of the selected cases were greater than or equal to 70 kt (Table 1). In addition to damaging winds, convection in each severe case also produced severe hail. Among the selected severe cases, the footprint of severe weather varied as well. For example, severe wind reports in case 2 spanned nearly five states over the course of around 18 h (Fig. 4b). Meanwhile, damaging wind reports in case 1 were

TABLE 1. List of representative cases including the peak estimated (E) and measured (M) wind gusts from StormData. Column 4 shows corresponding panels in Figs. 4–6 and 10, while column 5 corresponds to ASOS data displayed in Fig. 10.

Case No.	Date	Peak wind	Figure panels	Selected ASOS
1	12 Apr 2014	E75 kt	(a)	La Crosse, Wisconsin (KLSE)
2	4 May 2020	E96 kt; M77 kt	(b)	Lawrence, Kansas (KLWC)
3	15 Jun 2022	E83 kt; M78 kt	(c)	Hastings, Nebraska (KHSI)
4	12 May 2022	E70 kt; M66 kt	(d)	Rapid City, South Dakota (KRAP)
5	9 May 2022	E61 kt; M73 kt	(e)	Alliance, Nebraska (KAIA)
6	25 Mar 2021	M30 kt	(f)	Russellville, Arkansas (KRUE)

Brought to you by NOAA Central Library | Unauthenticated | Downloaded 08/28/24 03:27 PM UTC

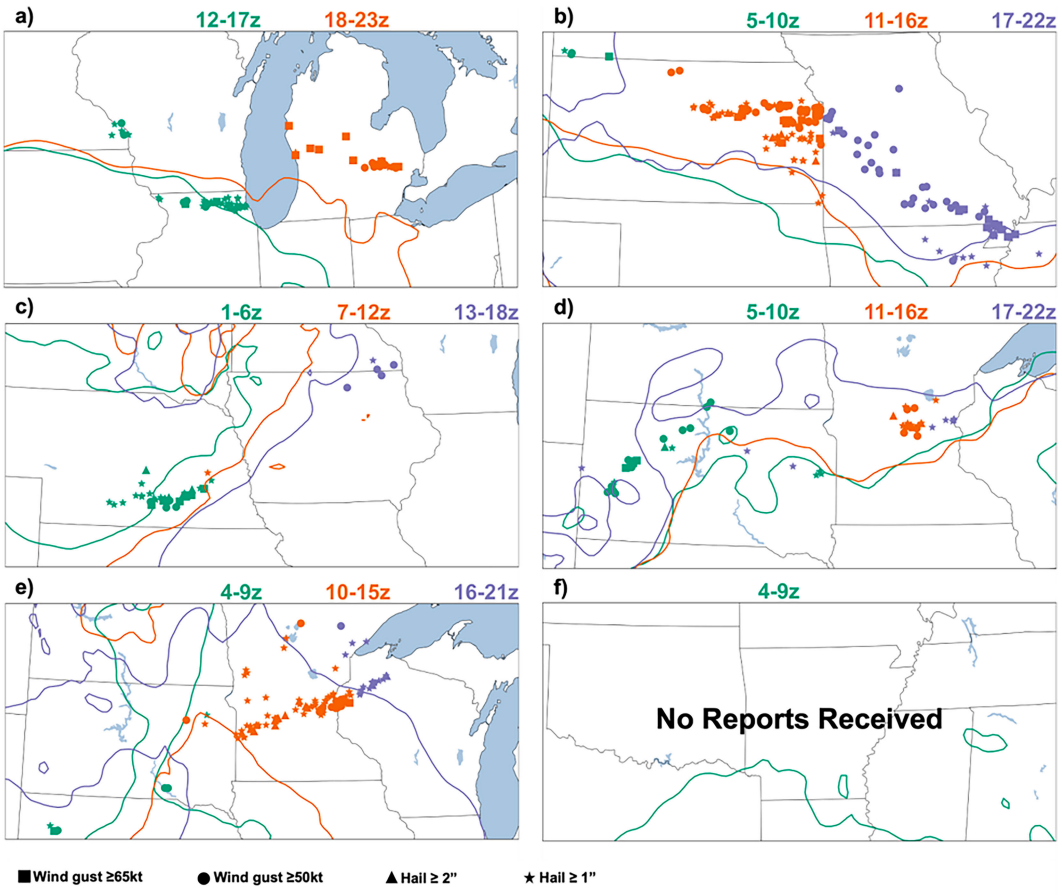

FIG. 4. Map of all reports of severe damaging wind and hail produced by elevated gravity wave coincident convection covering the approximate time periods of (a) 1200–2300 UTC 12 Apr 2014, (b) 0500–2200 UTC 4 May 2020, (c) 0100–1800 UTC 15 Jun 2022, (d) 0500–2200 UTC 12 May 2022, (e) 1000–2100 UTC 9 May 2022, and (f) 0000–2359 UTC 25 Mar 2021. The 5-h average northern extent of the 250 J kg^{-1} SBCAPE contours from the HRRR (Dowell et al. 2022) is shown with colors corresponding to individual times as shown by panel labels [except in (c), which shows the eastward extent]. The 5-h window of HRRR SBCAPE in (f) is valid when convection was present (see Fig. 5f). Stars indicate reports of hail (≥2.54 cm or 1 in. in diameter), triangles indicate reports of significant hail (≥5 cm or 2 in. in diameter), circles represent damaging winds (wind gusts ≥ 50 kt), and squares represent significantly damaging winds (wind gusts ≥ 65 kt).

confined to relatively small areas, associated with separate wave packets (not shown). Convective mode also differed between and within cases, ranging from single cell (case 2) to linear (cases 1–6) to supercellular (cases 1, 3, and 4). Case 2 was particularly varied, with multiple episodes of equally spaced convection and storm modes, including evidence that convection coincident with a gravity wave packet eventually became surface-based (not shown).

a. Radar signature

Regardless of whether surface damaging winds occurred, convection in each episode manifested as a single band or multiple equally spaced "arcing" bands of reflectivity with maximum values ranging from 50 dBZ to greater than 65 dBZ (Fig. 5). In some cases, multiple bands of equally spaced reflectivity developed and waned simultaneously while tracking repeatedly over the same areas throughout the duration of a convective episode. In other cases, an initially single band propagated for hundreds of miles, or at times was joined by multiple other equally spaced bands. Severe and nonsevere events appear similar in radar reflectivity structure, spacing, and intensity, providing little utility to anticipate or detect damaging wind production.

When damaging wind production appeared to be ongoing and convection was relatively close to a sampling radar, lowest-tilt base velocity data often demonstrated a divergence signature with paired, outward-oriented outbound and inbound returns and a relative minimum along the leading edge in radar reflectivity (Figs. 6a–d). Indeed, the mechanism for damaging wind production appeared to be along the leading edge of radar reflectivity, potentially close to convective-scale updrafts. Sometimes, the velocity returns exhibited a negative association with radar reflectivity, with the strongest velocities *ahead of* and weaker velocities *behind* the leading edge in

Brought to you by NOAA Central Library | Unauthenticated | Downloaded 08/28/24 03:27 PM UTC

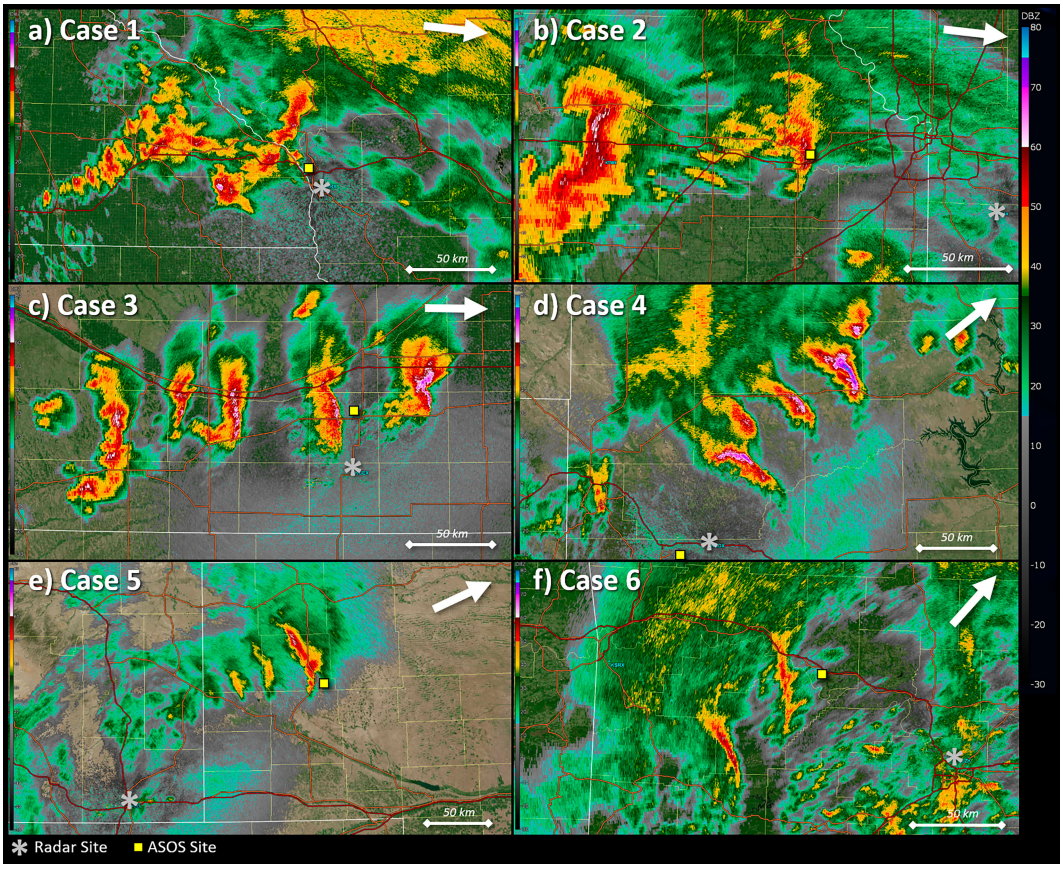

FIG. 5. The 0.5° radar reflectivity (dBZ) imagery from WSR-88D stations: (a) KARX at 1422 UTC 12 Apr 2014, (b) KEAX at 1457 UTC 4 May 2020, (c) KUEX at 0504 UTC 15 Jun 2022, (d) KUDX at 0803 UTC 12 May 2022, (e) KCYS at 0454 UTC 9 May 2022, and (f) KLZK at 0742 UTC 25 Mar 2021. Yellow squares indicate the location of ASOSs: (a) LSE—La Crosse, WI; (b) LWC—Lawrence, KS; (c) HSI—Hastings, NE; (d) RAP—Rapid City, SD; (e) AIA—Alliance, NE; and (f) RUE—Russellville, AR. Gray asterisks indicate the location of each respective radar, white arrows indicate the direction of convective motion, and white lines bounded by diamonds indicate a 50-km distance scale (differs for each panel).

radar reflectivity (e.g., Figs. 5a,c). Such a pattern would suggest that damaging winds are sometimes observed during a period void of precipitation, a pattern atypical of most traditional damaging wind production mechanisms in surface-based systems outside of systems that are outflow dominant.

When close to sampling radars, base velocity magnitudes provided meaningful insight into whether the convection was producing damaging surface winds, as returns $>$ 50 kt were often spatiotemporally associated with damaging wind reports. In comparison, many base velocity data in nondamaging cases displayed either a similar 0.5° base velocity divergence signature with returns $<$ 50 kt to those of damaging counterparts or little to no discernible change in surface flow direction or speed entirely (e.g., Fig. 6f). Accordingly, there were scenarios where the local environment supported surface wind production but not to severe levels. An analysis aimed at discriminating between environments that support damaging, nondamaging, and significantly damaging events is ongoing.

Cross sections through the regions of maximum velocity returns during damaging events demonstrated no clear connection to any midlevel momentum maximum within the convection, if present (i.e., a rear-inflow jet), and instead provided evidence of lifting a stable layer ahead of the convection. For example, a cross section taken through the maximum base velocity during convection in case 1 (Figs. 5 and 6a) showed an increase in surface flow apparently independent of other processes traditionally associated with the production of damaging surface winds (Figs. 7e,f). Indeed, the low-level stable layer—evident via easterly winds ahead of the convection—appeared to rise over surface winds by nearly 3 km and oscillate (Fig. 7f) as damaging wind production appeared to cease (Fig. 7d).

To demonstrate the typical evolution of a gravity wave coincident convective event, time steps of radar base reflectivity and velocity for case 4 are shown in roughly 30-min increments with reports of damaging wind and hail in Figs. 8 and 9. Initially, semidiscrete convective elements originated out of a region of low-level warm-air advection in proximity to an approaching, unrelated bore along the border of Wyoming and South Dakota and evolved into equally spaced bands of convection within a relatively narrow axis (Fig. 8). With time,

Brought to you by NOAA Central Library | Unauthenticated | Downloaded 08/28/24 03:27 PM UTC

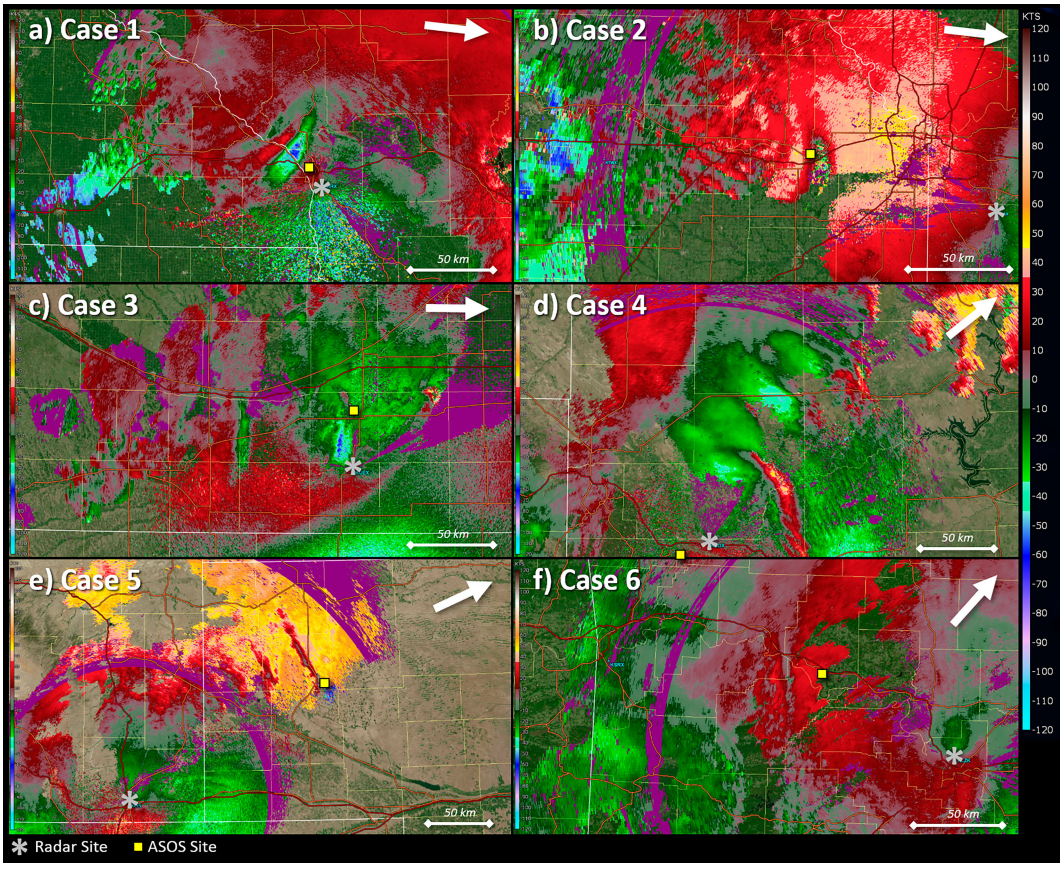

FIG. 6. As in Fig. 5, but with 0.5° base velocity (kt).

each band of convection developed a 0.5° base velocity divergence signature that corresponded with observed damaging surface wind production with inbound–outbound velocity couplets and relative minima at the leading edge in reflectivity (Figs. 9d,f). At times, the strongest base velocity values extended well outside the right edge (relative to forward motion) of radar reflectivity, which was confirmed as damaging by local storm reports along the right edge of each line segment (Figs. 8c–f). Such behavior has been observed across multiple convective events, with the majority of all reports of observed wind damage along the right flank of radar reflectivity. In addition, the convection produced numerous reports of damaging hail, as is typical with other cases (Fig. 4).

Because large areas of base velocity values associated with surface winds often appear ahead of the leading edge of radar reflectivity and indeed within an area of low power returned to a radar, operational forecasters may discount them as false or bad data. For one, the presence of velocity values ahead of a region of reflectivity can serve as a marker of sidelobe contamination in situations where a large vertical or horizontal gradient in reflectivity exists in convection (Boettcher and Bentley 2022). Theoretically, there may be situations in which sidelobe contamination exists within a region of real velocity values, particularly for a supercell storm mode or in convection with steep vertical gradients in reflectivity. As a result, care must be taken when diagnosing real base velocity values in regions of relatively low reflectivity. A relatively smooth increase and broad area of base velocity values should give confidence that the signature is not indicative of sidelobe contamination (Figs. 7c,d provide clear examples).

Similar to other radar-based signatures, the maxima in base velocity returns can be difficult to discern or undetectable owing to a lack of scatterers (e.g., Fig. 6b) or a poor viewing angle with respect to the location of the sampling radar. In addition, the signature may not be visible at great distances from sampling radars (e.g., Fig. 6e). At least a subtle signature of divergence along the leading edge of reflectivity has been noted as far away as ~100 mi (~160 km) and at a height of 10 000 ft (~3 km) from a sampling radar (e.g., Fig. 9f). Even so, the distance at which the divergence signature may be apparent, or the magnitude of winds entirely, may be dependent on environmental variables requiring additional analysis outside the scope of this study. Finally, the choice of color table or use of storm-relative velocity may also limit the ability to identify the base radar divergence signature, as well.

b. Surface observation pattern

In each of the six representative cases, convection passed directly over or close to ASOS stations, allowing for a comparison of temperature, pressure, wind, and precipitation data

Brought to you by NOAA Central Library | Unauthenticated | Downloaded 08/28/24 03:27 PM UTC

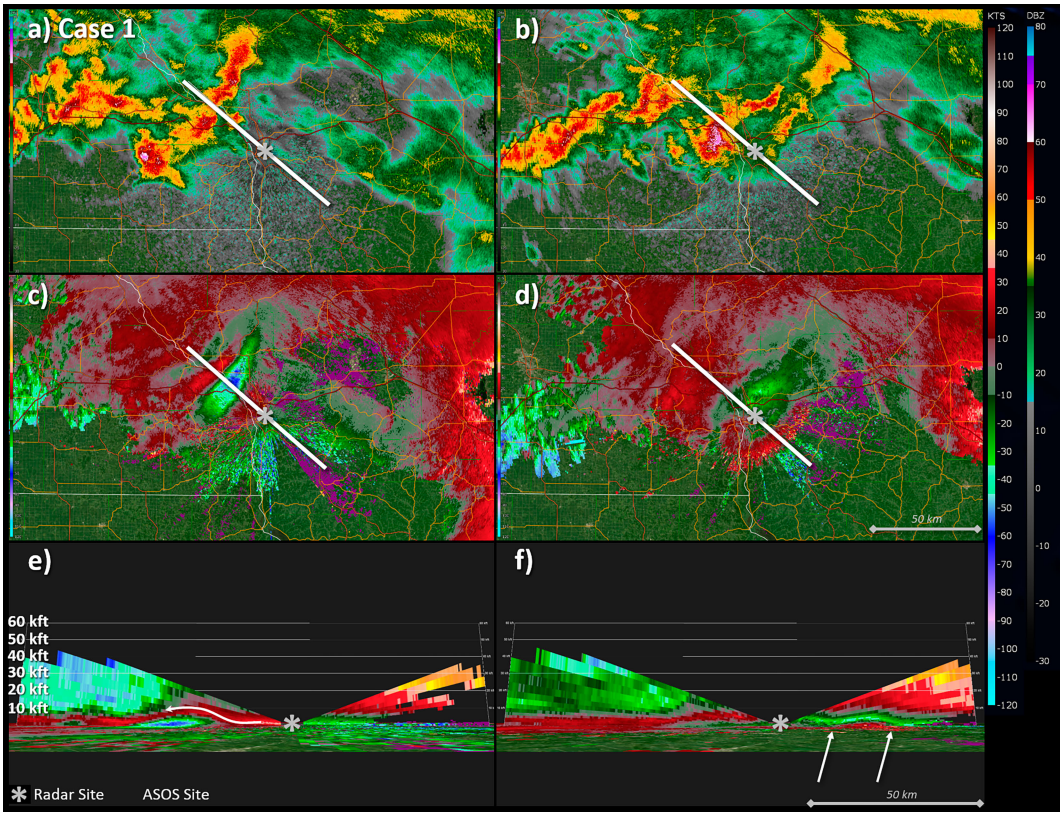

FIG. 7. Radar data from KARX at (a),(c),(e) 1422 UTC and (b),(d),(f) 1450 UTC 14 Apr 2014. (a),(b) The 0.5° base reflectivity (dBZ); (c),(d) 0.5° base velocity (kts). (e),(f) Cross sections of base velocity (kt) along the white lines shown in (a)–(d). The white arrow in (e) shows the implied vertical windflow, while the white arrows in (f) indicate wave oscillations in the surface stable layer. Gray asterisks indicate the location of KARX in (a)–(f), and gray lines bounded by diamonds indicate a 50-km distance reference in (d) [applicable for (a)–(c)] and (f) [also applicable for (e)].

between events. Observational data from ASOSs at a 1-min resolution were downloaded and plotted for 2-h windows during which convection passed overhead (Figs. 5 and 6), as shown in Fig. 10. Among the six cases, several representative observational patterns emerge. For example,

- The sustained winds and gusts produced by the convection were associated with abrupt surface pressure oscillations of 2–6 mb (1 mb = 1hPa) over 5–10 min, with sustained wind and gust magnitudes peaking close to or just after the peak in surface pressure or as the surface pressure started to fall. In other words, the peak in surface winds did not occur as the surface pressure was rising. In situations during which multiple bands of convection passed over the ASOS, several associated oscillations in pressure and winds were evident (e.g., Figs. 10c,f).
- While the pressure oscillated during the period of convective winds, observed temperatures remained nearly steady or increased by 1°–2°C outside of external influences such as a nearby cold front. Such behavior would not be expected with traditional gravity-current or downburst-driven damaging winds, which are typically accompanied by pressure rises and temperature falls (e.g., Haertel et al. 2001). Given negligible changes in surface dewpoint temperatures during surface wind production (not shown), the observational pattern may not be indicative of penetrative convective downdrafts or heat bursts (e.g., Bernstein and Johnson 1994).[10]
- The convective wind gusts were associated with shifts in wind direction that matched the direction of convective motion and wave propagation. Once the convective wind gusts ended (and, often, precipitation began), the wind direction veered and, in several cases, reverted to the direction prior to convective wind gusts.
- The observed timing of severe surface wind production aligned with when the base velocity maxima passed directly overhead and often before the leading edge of radar reflectivity arrived. Indeed, surface winds may be accompanied by little to no rainfall (Figs. 10c–e).

[10] It is worth noting that the damaging winds measured just before 0515 UTC in case 3 (e.g., Fig. 10c) were associated with a decrease in dewpoint. However, the other periods of surface wind production shown (e.g., just before 0430 UTC and 0600 UTC) were associated with negligible changes in dewpoint.

Brought to you by NOAA Central Library | Unauthenticated | Downloaded 08/28/24 03:27 PM UTC

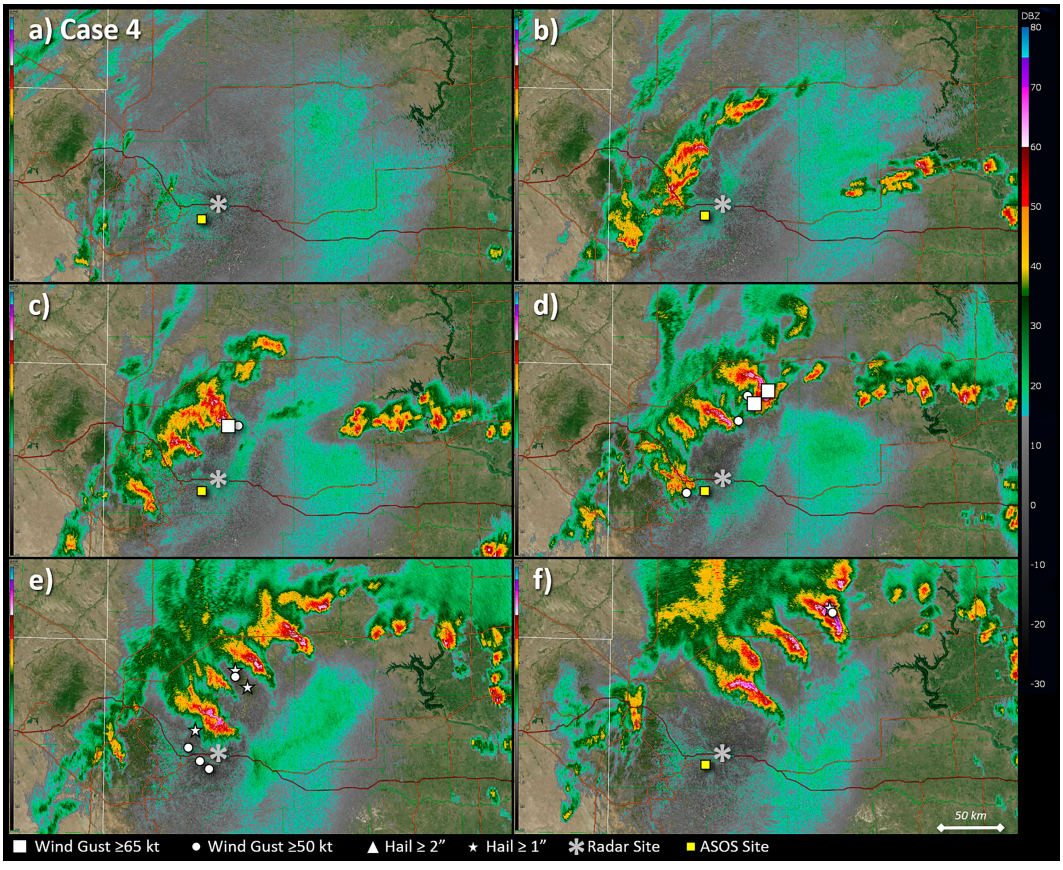

FIG. 8. The 0.5° radar reflectivity (dBZ) imagery from KUDX at (a) 0531 UTC, (b) 0606 UTC, (c) 0633 UTC, (d) 0702 UTC, (e) 0737 UTC, and (f) 0803 UTC 12 May 2022. Damaging wind and hail reports are plotted when reported 35 min prior to each respective scan with the same convention as Fig. 4. Yellow squares indicate the location of the Rapid City, SD, ASOS, while gray asterisks indicate the location of KUDX. The white line in (f) indicates a 50-km reference distance.

- In case 6, where damaging winds were not observed or reported with two successive waves (e.g., Fig. 5f), the pressure and nonsevere winds nevertheless remained associated, the wind direction changed as each pressure wave moved overhead, and the temperature remained nearly steady. Base velocity data did not indicate any notable increase in wind speed with each wave, contrary to ASOS observations (cf. Figs. 6f and 10f).

The absence of temperature falls during the time period of associated pressure rises and convective wind generation, as well as the peak wind and gust magnitudes taking place near or just after the peak in pressure, suggests that cold-pool or rear-inflow jet processes that are traditionally responsible for damaging wind production in surface-based convection were not present in the six representative cases. Rather, the observational patterns displayed by the ASOSs impacted by each representative case were consistent with observations of a similar convective event cataloged by C21 and simulated by S23, who determined the process responsible for damaging surface winds was the breaking of MGWs along the leading edge of elevated convection. In fact, C21 noted a sharp temperature increase along with pressure fluctuations of nearly 5 mb in 19 s as convective wind gusts were ongoing, suggesting the full magnitude and detail of meteorological data may not have been adequately captured by the 1-min resolution of each ASOS in the representative cases. As a result, it appears worthwhile to investigate the linkage between mesoscale gravity waves and damaging wind production in the cases identified herein.

4. Association with up–down trajectories

To provide context on the frequency of occurrence of the mechanism by which elevated convection can produce damaging winds identified by S23 and provide a link to the observations of the representative cases, case 4 was simulated using version 4.0.3 of the Advanced Research version of the Weather Research and Forecasting (WRF-ARW) Model (Powers et al. 2017). The simulation was initialized at 0000 UTC 12 May 2022 with High-Resolution Rapid Refresh (HRRR) hourly forecast output used as initial and lateral boundary conditions. The simulation used a nested grid, with the outer domain at 3-km grid spacing and the inner domain at 600-m grid spacing (Fig. 11).

Brought to you by NOAA Central Library | Unauthenticated | Downloaded 08/28/24 03:27 PM UTC

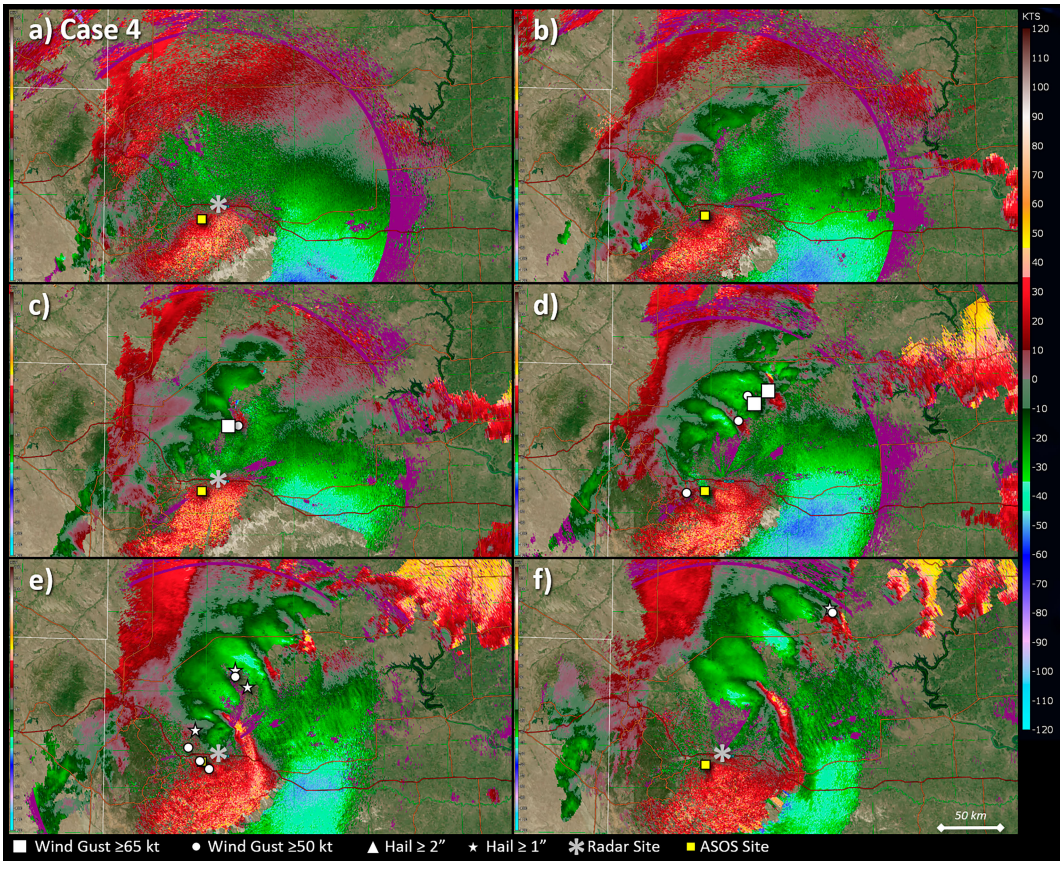

FIG. 9. As in Fig. 8, but with 0.5° base velocity (kt).

The vertical grid included 85 levels, stretched to have higher resolution in the planetary boundary layer. The time step was 15 s on the outer domain and 3 s on the inner nest. Like in S23, the physical parameterizations included the Thompson et al. (2008) two-moment cloud microphysics parameterization, the Mellor–Yamada–Janjić (MYJ; Mellor and Yamada 1982; Janjić 2001) planetary boundary layer parameterization, the Rapid Radiative Transfer Model for general circulation models (GCMs; Iacono et al. 2008), and the Noah (Chen and Dudhia 2001) land surface model. A reference forecast sounding taken as convection was ongoing is shown in Fig. 12.

The evolution of the simulated convection is shown in Fig. 13. Qualitatively speaking, convection in the simulation developed and evolved similarly to what was observed within equally spaced bands across western and northern South Dakota (cf. Figs. 8 and 13). The simulated convection did not produce severe surface winds that were as widespread as those observed, as there were broad swaths of wind speeds exceeding 35 kt, but only isolated locations where the wind exceeded 50 kt (Fig. 13). In addition, simulated convection appeared to evolve slower than what was observed, with the most obvious banded structures in simulated convection evident at 1000 UTC (Fig. 13d) compared to the observed wave-like structures between 0700 and 0800 UTC (Figs. 8e,f). Even with differences in timing and magnitude of damaging winds between the observed and simulated systems, the overall qualitative similarities between the two suggest the simulation likely captured the mechanisms driving the convection and observed damaging winds.

Similar to the observations measured by the ASOS at Rapid City, South Dakota (KRAP), and damaging-wind-producing elevated convection documented by C21 and simulated in S23, time series from the simulation at a location where damaging surface winds were simulated (e.g., Fig. 13d) shows abrupt increases in surface pressure and temperature on the order of 5–7 mb and 2°–3°C, respectively, along with strong surface wind production and associated temporary wind shifts that match the direction of convective propagation, particularly at 1000 UTC and just after 1100 UTC (cf. Figs. 10d and 14 with Figs. 2 and 8 from S23). In addition, each individual band of simulated convection appeared to repeat the observational patterns documented in other cases (e.g., case 3; Fig. 10c) when several individual convective bands moved over the ASOS.

As in S23, planar views of the simulated convection in case 4 revealed a wave-like structure with arcing ribbons of high pressure along the leading edge of reflectivity ranging from 5 to 10 mb higher than bounding regions of lower pressure outside of convection, collocated with subtle increases in surface potential temperature of 1–2 K near regions of surface wind production (cf. Fig. 15 with Fig. 6 of S23). Meanwhile,

Brought to you by NOAA Central Library | Unauthenticated | Downloaded 08/28/24 03:27 PM UTC

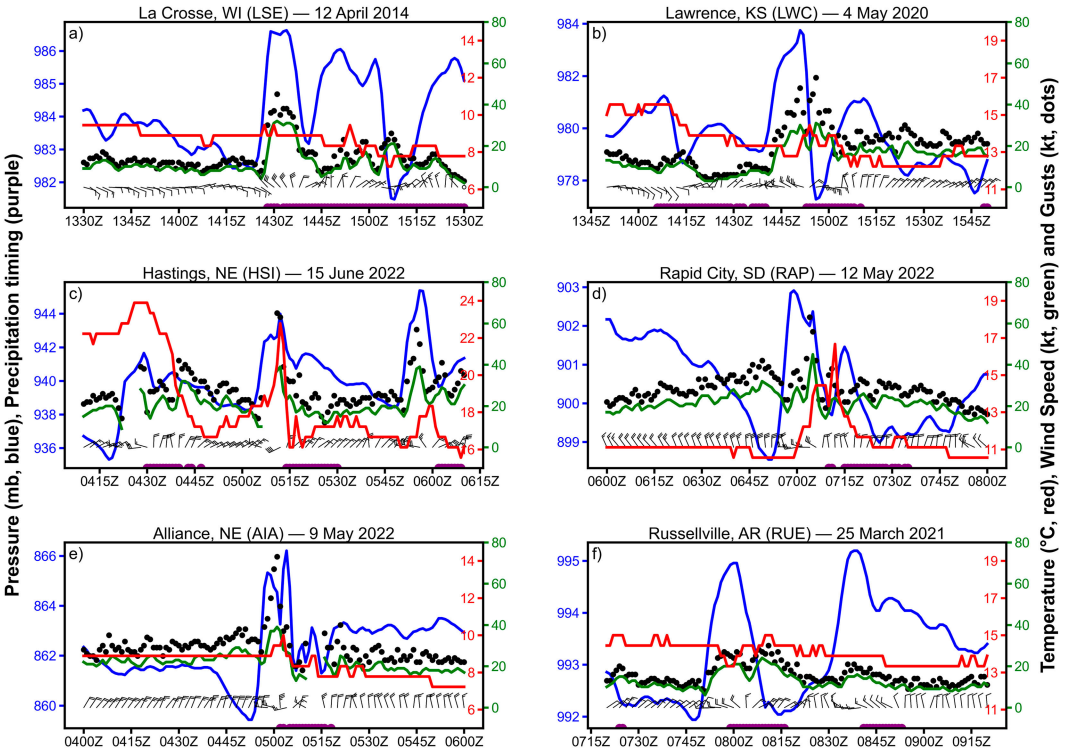

FIG. 10. Time series of temperature (red contour; °C), pressure (blue contour; mb), 10-m wind speed (green contour; kt), wind gust (black dots; kt), and wind barbs (half barb = 5 kt and full barb = 10 kt) sampled at ASOSs over a 2-h window from (a) LSE—La Crosse, WI, between 1330 and 1530 UTC 12 Apr 2014; (b) LWC—Lawrence, KS, between 1345 and 1545 UTC 4 May 2020; (c) HSI—Hastings, NE, between 0415 and 0615 UTC 15 Jun 2022; (d) RAP—Rapid City between 0600 and 0800 UTC 12 May 2022; (e) AIA—Alliance, NE, between 0400 and 0600 UTC 9 May 2022; and (f) RUE—Russellville, AR, between 0715 and 0915 UTC 25 Mar 2021. Purple markings at the bottom of each panel indicate observation times for which rain was reported at each ASOS site.

potential temperature deficits of 4–8 K were located atop the region of aforementioned surface pressure rises (Fig. 15d). Like in S23, a surface pattern from low to high to low pressure in a region void of a surface cold pool and beneath a region of relatively cooler potential temperatures suggests the convection was associated with MGWs.

A cross section taken through the simulated convection further implicates the association of MGWs with the banded convective elements given two instances of upward- and downward-bending pseudoisentropes out of phase with convective updrafts and downdrafts (near $x = -101.00$ and -99.80 in Fig. 16a). Given that the pseudoisentropes provide an approximate pathway of ambient low-level air that encounters the MGWs, one can envision a theoretical parcel airflow that first rides atop the crest of each wave only to rapidly descend downward as a downburst where the pseudoisentropes become nearly vertical, consistent with up–down trajectories. Indeed, there is evidence of surface divergence and associated downbursts at the bases of each downward branch of the gravity waves, especially with the leading wave, similar to what was simulated in S23 (e.g., cf. Fig. 16b with Fig. 7 of S23). However, unlike in S23, there was no clear evidence of gravity wave breaking in the simulation of case 4 given that the pseudoisentropes did not appear to overturn on the downward branch of each gravity wave. We speculate that these factors are responsible for the relatively muted rises in surface pressure, temperature, and wind speed in the simulation of case 4 when compared to those observed or simulated by damaging-wind-producing elevated convection in C21 and S23. In other words, it appears that the breaking of gravity waves may be required for extreme but not necessarily severe winds. Such a relationship is worthy of additional analysis that is outside the scope of this study. Nevertheless, the simulation of case 4 appears to directly tie the downward branch of gravity waves to the generation of a downburst and surface severe wind generation, similar to the airflow depicted in Fig. 20 of S23.

Given the similarities in observations of associated surface pressure and temperature rises during periods of damaging winds and equally spaced reflectivity structures indicative of MGWs across all representative damaging cases (e.g., Fig. 10), damaging winds associated with the downbursts on the downward branch of MGWs associated with convection may occur with regularity across a range of convective environments, locations, and times of the day and year.

5. Concluding remarks and future work

Elevated convection has long been thought to primarily pose a threat for damaging hail. However, a growing body of

Brought to you by NOAA Central Library | Unauthenticated | Downloaded 08/28/24 03:27 PM UTC

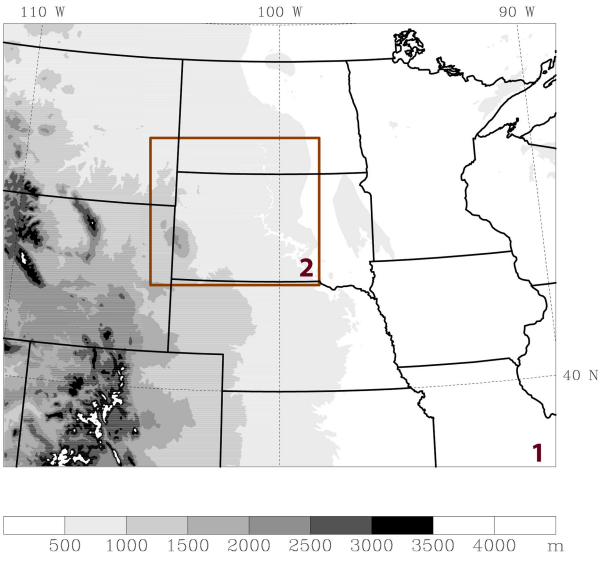

FIG. 11. Map of the WRF-ARW model domains. The locations of domains 1 and 2 are shown, and terrain (m) is shaded.

evidence suggests elevated convection, especially that associated with MGWs, can and often does produce damaging surface winds that can pose a substantial threat to lives and property. Unlike surface-based convection that produces damaging winds through downbursts, descending rear-inflow jets, and mesovortices, elevated convection is thought to produce damaging winds through a unique process of dynamically lifting and dropping a near-surface layer. The predominant method to facilitate such up–down trajectories is beyond the scope of this study, but it could be through 1) updrafts and downdrafts associated with gravity waves (e.g., S23), 2) the vertical accelerations associated with perturbation pressure gradients induced by the updrafts of elevated supercells (e.g., MacIntosh and Parker 2017), or—perhaps—3) a combination thereof or an entirely different method. Regardless, observational evidence supplied by radar data suggests that the theoretical process of up–down trajectories occurs with an identifiable and actionable radar signature, perhaps with some degree of regularity. To the knowledge of the authors, the cases presented herein are the first documentation of radar observations suggesting up–down trajectories as means to describe the generation of damaging surface winds by elevated convection.

Key radar and observational features of MGW-coincident damaging-wind-producing elevated convection include the following:

- Single or multiple equally spaced arcing bands of convection with divergent couplets of 0.5° base velocity centered along the leading edge of reflectivity with observed damaging winds along the rightward side of convective elements relative to storm motion
- Cross sections taken through divergent couplets in base velocity depict a separation of midlevel convective momentum and

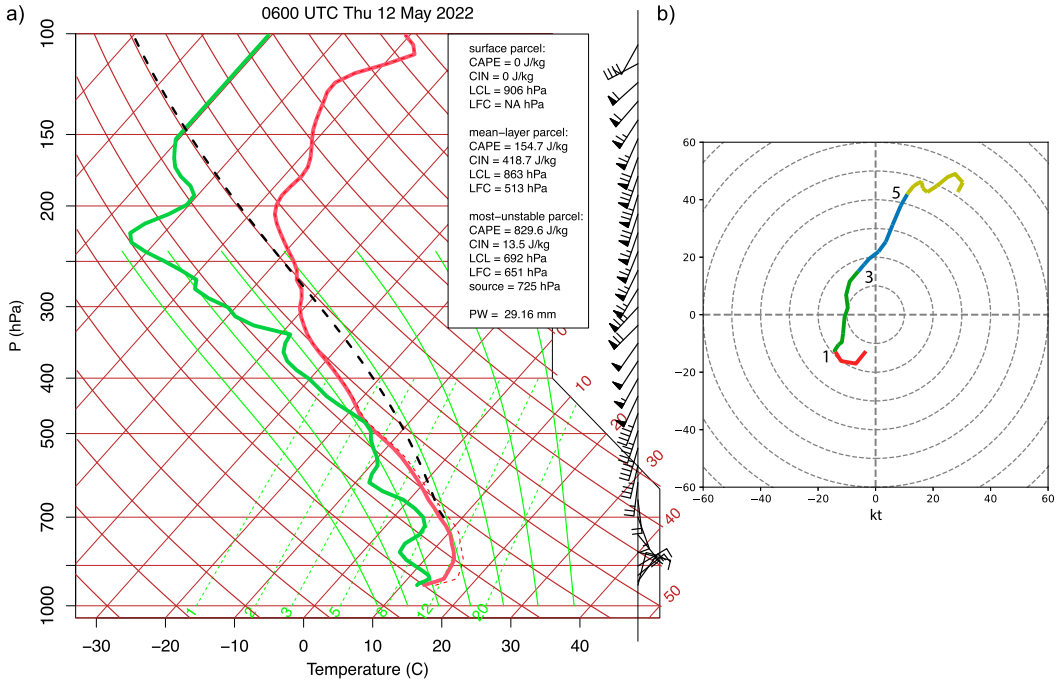

FIG. 12. Vertical profile of WRF forecast at 0600 UTC 12 May 2022 immediately ahead of the simulated convection, as shown in Fig. 13. (a) Skew T–log$p$ diagram of temperature (red; °C), dewpoint (green; °C), and winds (barbs; half barb indicate winds of 5 kt, full barbs indicate 10 kt, and pennants indicate 50 kt). The black dashed line represents the temperature of the most unstable parcel. (b) Hodograph of winds (kt) in the lowest 8 km AGL of the profile, with the color changing at 1, 3, and 5 km AGL.

Brought to you by NOAA Central Library | Unauthenticated | Downloaded 08/28/24 03:27 PM UTC

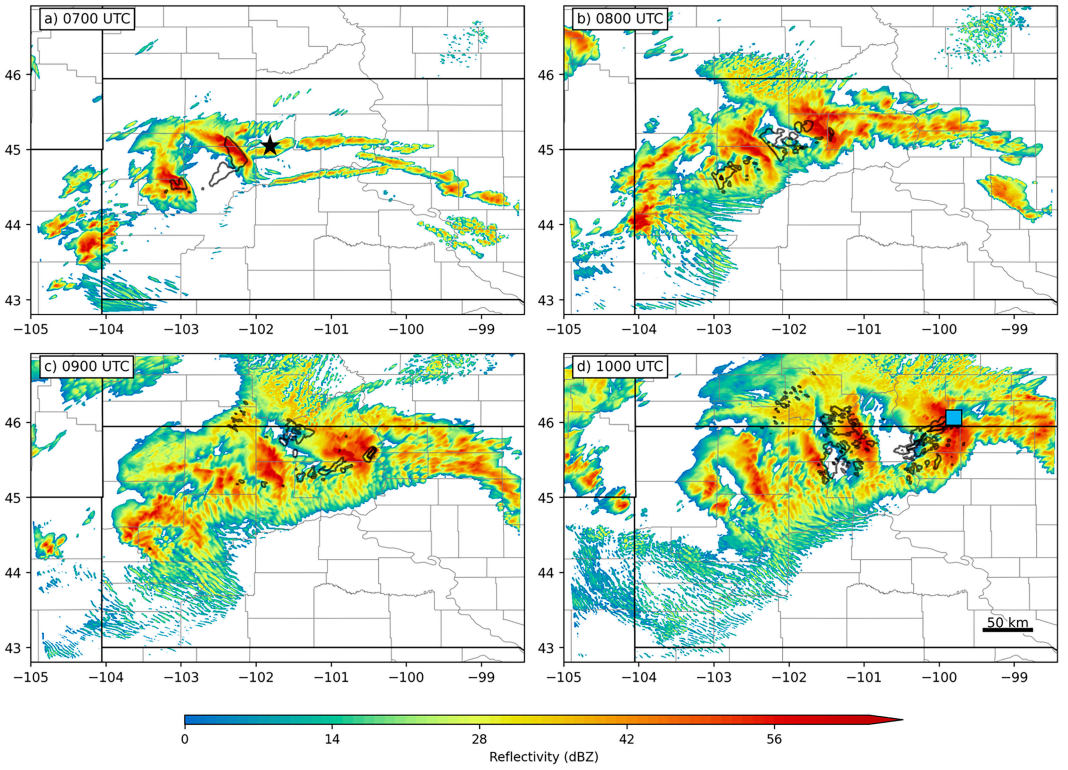

FIG. 13. Simulated 1-km radar reflectivity (dBZ; shaded) and 10-m wind speed (contoured in gray at 35 kt and black at 50 kt) at (a) 0700 UTC, (b) 0800 UTC, (c) 0900 UTC, and (d) 1000 UTC from the WRF-ARW simulation. The black star in (a) represents the location of a skew T–log$p$ diagram shown in Fig. 12, and the blue box in (d) represents the location of a pseudo-ASOS for which observations are shown in Fig. 14.

the lifting of the near-surface stable layer ahead of the convection itself

- Associated surface pressures, sustained winds, and wind gusts during damaging wind production with little to no change in surface temperature, and abrupt shifts in wind directions to match the direction of convective propagation

While 0.5° base velocity signatures can provide insights into damaging and nondamaging MGW convective events, future work is needed to determine if other radar variables such as isothermal reflectivity or dual-polarization fields can provide skill in discriminating severe from nonsevere events. In addition, the creation of automated methods to identify equally

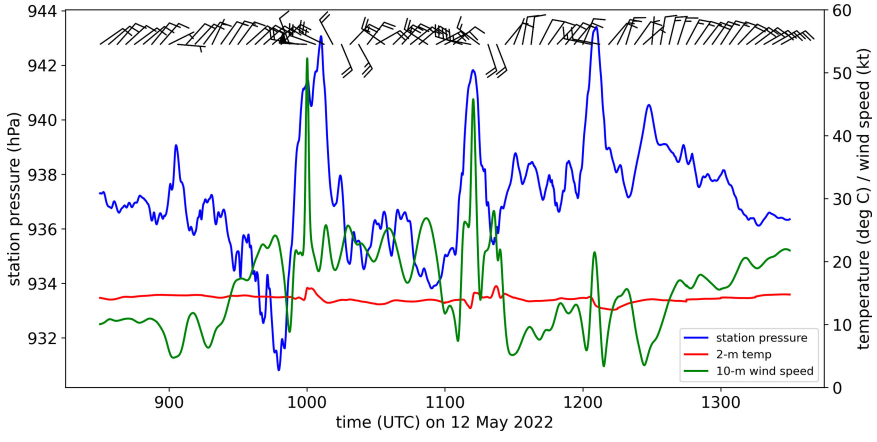

FIG. 14. Time series of temperature (red contour; °C), station pressure (blue contour; hPa), 10-m wind speed (green contour; kt), and wind barbs (half barb = 5 kt and full barb = 10 kt) from the WRF simulation at the location shown in Fig. 13d. Values were extracted at each model time step and are shown from 0830 to 1130 UTC 12 May 2022.

Brought to you by NOAA Central Library | Unauthenticated | Downloaded 08/28/24 03:27 PM UTC

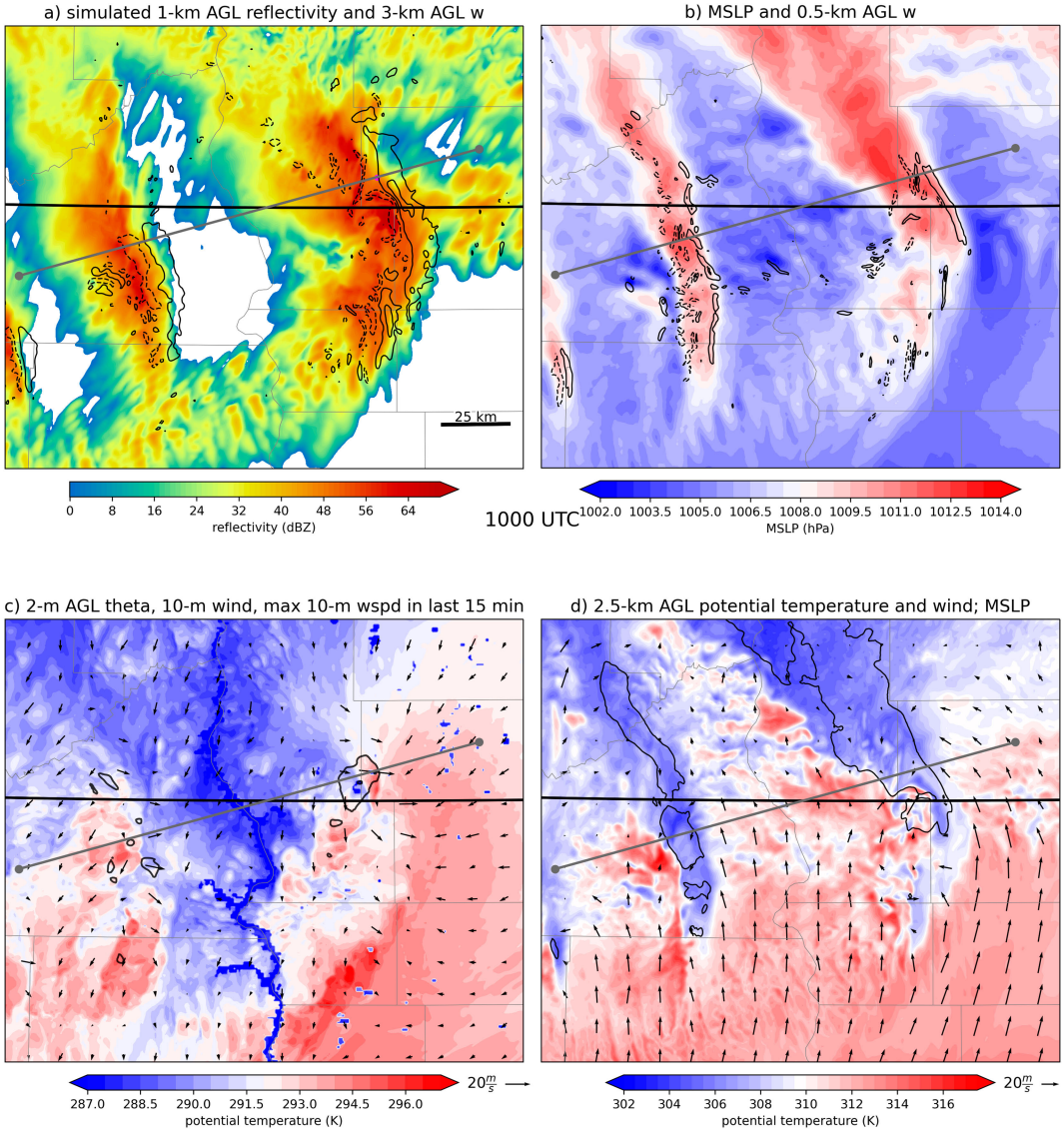

FIG. 15. Output from the WRF simulation at 1000 UTC. (a) Simulated radar reflectivity at 1 km AGL (dBZ; shaded) and vertical velocity at 3 km AGL (black contours every at ±5 and 15 m s^{-1}; negative values dashed); (b) mean sea level pressure (hPa; shaded) and vertical velocity at 500 m AGL (black contours every 3 m s^{-1}; negative values dashed); (c) potential temperature at 2 m AGL (K; shaded), maximum 10 m AGL wind speed in the previous 15 min (black contours at 20 and 30 m s^{-1}), and 10-m wind vectors; and (d) potential temperature at 2.5 km AGL (K; shaded), mean sea level pressure (black contours at 1010 and 1015 hPa), and 2.5 km AGL wind vectors. The gray line shows the location of the vertical cross sections shown in Fig. 16.

spaced bands of convection, including the presence of a 0.5° base velocity divergence signature, may prove useful to identify damaging events as they are ongoing and complement those already developed to identify MGWs by themselves (e.g., Koch and Saleeby 2001). Also, a more thorough analysis of storm mode and report type may provide clues to the dominant mechanism to facilitate damaging surface winds in elevated convection.

In addition, efforts should be made to better quantify the frequency of MGW convective events with respect to other "types" of severe and nonsevere convective episodes. With 52 events cataloged over a 2-yr period, MGW convective events only make up a small component of all convective episodes on an annual basis, though they may make up a relatively large component of unwarned or unexpected severe weather events. Indeed, quantifying the proportion of severe MGW events or damage reports that are unwarned, or occur outside the bounds of severe weather forecasts such as those prepared by the Storm Prediction Center, may prove insightful.

While not explicitly explored in the present manuscript, convective MGWs share a diversity in character with different widths of spacing between convective bands, location with

Brought to you by NOAA Central Library | Unauthenticated | Downloaded 08/28/24 03:27 PM UTC

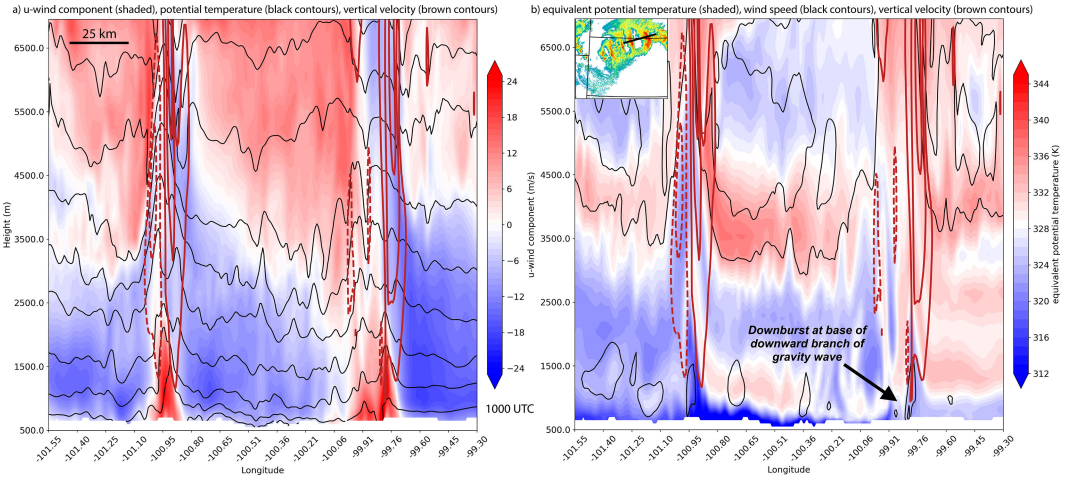

FIG. 16. Vertical sections through the line shown in Fig. 15 at 1000 UTC of the WRF simulation showing (a) zonal wind component (m s^{-1}; shaded), potential temperature (black contours every 4 K), and vertical velocity (brown contours every 5 m s^{-1}; negative contours dashed); and (b) equivalent potential temperature (K; shaded), wind speed (black contours every 10 m s^{-1} starting at 20), and vertical velocity (brown contours every 5 m s^{-1}; negative contours dashed). Location of the vertical section overlain on simulated reflectivity shown in the top left of (b).

respect to frontal boundaries and synoptic-scale systems, and initial formation mechanisms (both with respect to MGWs and the convection themselves). Do the mechanisms through which the elevated convection and MGWs develop matter? Are certain types of MGWs that become, or are intrinsically tied to, elevated convection more conducive to supporting damaging surface winds? Moreover, what types of environments and MGWs are more likely to *break*, potentially supporting *extreme* damaging winds? Additional work, particularly through the use of numerical model simulations, is needed to parse out the nuanced relationships between MGWs and damaging-wind-producing convection.

Finally, while identifying radar and observational signatures associated with damaging surface winds produced by elevated convection may help reduce future missed events by providing a signal that a convective warning is needed, there are limited, if any, methods to *forecast* an event before it occurs. Early work examining operational convective-allowing model (CAM) output leading up to elevated convective episodes suggests at least some discriminatory skill in resolving equally spaced banded convection and even separating severe and nonsevere events. Moreover, early analyses of environmental parameters suggest qualitative similarities in environments supportive of severe events. However, more work is needed to determine explicit forecast skill in CAM guidance and to parse out potentially nuanced relationships in environmental parameters supportive of, and perhaps discriminatory between, different magnitudes of damaging winds produced by elevated convection.

Acknowledgments. The authors graciously acknowledge Bob Dukeshere, Cort Scholten, T. J. Turnage, Paul Schlatter, and Phil Schumacher for initial case identification and discussions that ultimately motivated this study. In addition, the authors thank W. Scott Lincoln, Kevin Donofrio, Matthew Bunkers, Jeffrey Manion, and James Ruppert, as well as two anonymous reviewers, who provided thoughtful comments and recommendations that greatly improved this manuscript. Finally, the authors acknowledge Brian K. Blaylock for his Herbie Python package used in the creation of Fig. 4.

Data availability statement. All radar and observational data used in this study are available from the National Centers for Environmental Information (https://www.ncei.noaa.gov/). High-Resolution Rapid Refresh output used to initialize the WRF model was obtained from the Amazon Web Services archive (https://noaa-hrrr-bdp-pds.s3.amazonaws.com/index.html). Initialization files and namelists required to reproduce the WRF simulations are available in the Dryad repository at https://doi.org/10.5061/dryad.tdz08kq5w. The full model output will be made available upon request to Russ Schumacher.

APPENDIX

List of Cases Used in This Study

Table A1 provides a full list of cases used in the 2-yr climatology, in addition to eight additional cases collected through operational experience.

Brought to you by NOAA Central Library | Unauthenticated | Downloaded 08/28/24 03:27 PM UTC

TABLE A1. Table of the 52 cases in the 2021–22 climatology and additional eight cases used in this study by year (YYYY), month (MM), day (DD), approximate start and end times, generic geographic region, peak measured (M) or estimated (E) wind gust (kt), peak hail size (in.), and wind classification, as described in the text (Pot. Dam. = potentially damaging; Sig. Dam. = significantly damaging; Dam. = damaging). Cases listed with an "*" were not included in the climatology presented in section 2.

Case No.	YYYY	MM	DD	Start time	End time	Region	Peak wind	Peak hail	Wind classification
1	2022	11	11	1200 UTC 11/11	0000 UTC 11/12	Southern Plains	—	1.75 in.	Pot. Dam.
2	2022	11	3–4	0200 UTC 11/4	2200 UTC 11/4	Mississippi River valley	M56 kt	1.25 in.	Dam.
3	2022	9	19	1500 UTC 9/19	2000 UTC 9/19	Northern Plains	—	1.50 in.	Null
4	2022	9	17–18	0000 UTC 9/18	1400 UTC 9/18	Northern Plains	—	—	Null
5	2022	9	9–10	0300 UTC 9/10	0700 UTC 9/10	Northern Plains	—	—	Null
6	2022	9	8–9	0230 UTC 9/9	1800 UTC 9/9	Great Lakes	—	0.88 in.	Null
7	2022	8	19–20	0000 UTC 8/20	1000 UTC 8/20	Southern Plains	—	—	Null
8	2022	6	19	0600 UTC 6/19	1700 UTC 6/16	Northern Rockies	M79 kt	1.75 in.	Sig. Dam
9	2022	6	14–15	0200 UTC 6/15	1900 UTC 6/15	Central Plains	E83 kt	2.50 in.	Sig. Dam.
10	2022	6	10–11	0100 UTC 6/11	0900 UTC 6/11	Northern Plains	—	—	Null
11	2022	6	9–10	2000 UTC 6/9	1000 UTC 6/10	Central Plains	E61 kt	1.75 in.	Dam.
12	2022	5	30–31	0400 UTC 5/31	1900 UTC 5/31	Central Plains	—	—	Null
13	2022	5	20–21	2100 UTC 5/20	1800 UTC 5/21	Mississippi River valley	M54 kt	—	Dam.
14	2022	5	15	0600 UTC 5/15	1900 UTC 5/15	Central Plains	E65 kt	1.75 in.	Sig. Dam.
15	2022	5	11–12	0400 UTC 5/12	1200 UTC 5/12	Northern Plains	E70 kt	1.75 in.	Sig. Dam.
16	2022	5	8–9	2230 UTC 5/8	1730 UTC 5/9	Northern Plains	M73 kt	3.00 in.	Sig. Dam.
17	2022	4	27–28	0300 UTC 4/28	1200 UTC 4/28	Southern Plains	M56 kt	1.00 in.	Dam.
18	2022	4	15–16	0400 UTC 4/16	1700 UTC 4/16	Southern Plains	E61 kt	1.00 in.	Dam.
19	2022	4	12	1800 UTC 4/12	0000 UTC 4/13	Great Lakes	E61 kt	1.75 in.	Dam.
20	2022	3	17–18	0400 UTC 4/18	0900 UTC 4/18	Great Lakes	—	—	Pot. Dam.
21	2022	2	21–22	0100 UTC 2/22	0600 UTC 2/22	Southern Plains	—	1.75 in.	Pot. Dam.
22	2021	12	26–27	0200 UTC 12/27	1000 UTC 12/27	Great Lakes	—	—	Null
23	2021	10	25	1200 UTC 10/25	1700 UTC 10/25	Northeast	—	—	Null
24	2021	10	19–20	2300 UTC 10/19	1500 UTC 10/20	Central Plains	—	0.88 in.	Null
25	2021	10	10	1700 UTC 10/10	0600 UTC 10/11	Southern Plains	M52 kt	—	Dam.
26	2021	9	28	0000 UTC 9/28	0300 UTC 9/28	Central Plains	—	—	Null
27	2021	9	20	0000 UTC 9/20	0600 UTC 9/20	Central Plains	M55 kt	—	Dam.
28	2021	8	20	0200 UTC 8/20	1000 UTC 8/20	Central Plains	—	—	Null
29	2021	7	14	1800 UTC 7/14	0200 UTC 7/15	Great Lakes	—	—	Null
30	2021	7	13	1700 UTC 7/13	0000 UTC 7/14	Northern Plains	M67 kt	—	Sig. Dam.
31	2021	6	19–20	0000 UTC 6/20	0800 UTC 6/20	Northern Plains	M46 kt	—	Pot. Dam.
32	2021	6	15	0600 UTC 6/15	1500 UTC 6/15	Pacific Northwest	—	1.50 in.	Null
33	2021	6	13–14a	2100 UTC 6/13	1000 UTC 6/14	Great Lakes	E52 kt	0.75 in.	Dam.
34	2021	6	13–14b	0000 UTC 6/14	0800 UTC 6/14	Pacific Northwest	—	—	Null
35	2021	6	5–6	0300 UTC 6/6	1200 UTC 6/6	Northern Plains	—	1.00 in.	Null
36	2021	5	8	0200 UTC 5/8	0700 UTC 5/8	Ohio River valley	—	—	Null
37	2021	5	5–6	0000 UTC 5/6	0800 UTC 5/6	Southern Plains	—	1.25 in.	Null
38	2021	5	4	1700 UTC 5/3	0400 UTC 5/4	Southern Plains	—	0.88 in.	Null
39	2021	5	1	2100 UTC 5/1	0500 UTC 5/1	Northern Plains	M55 kt	—	Dam.
40	2021	4	27–28	0600 UTC 4/27	1300 UTC 4/28	Great Lakes	—	1.25 in.	Null
41	2021	4	19	0900 UTC 4/19	1800 UTC 4/19	Northeast	—	1.00 in.	Null
42	2021	4	15–18	0900 UTC 4/15	1500 UTC 4/18	Gulf Coast	E50 kt	2.50 in.	Dam.
43	2021	4	12	2300 UTC 4/12	0400 UTC 4/13	Southern Plains	—	—	Null
44	2021	3	26	0000 UTC 3/27	0600 UTC 3/27	Central Plains	E55 kt	1.00 in.	Dam.
45	2021	3	24–25	0200 UTC 3/25	1500 UTC 3/25	Mississippi River valley	—	2.00 in.	Null
46	2021	3	16–17	0000 UTC 3/17	0800 UTC 3/17	Southern Plains	E74 kt	1.75 in.	Sig. Dam.
47	2021	3	13	1200 UTC 3/13	0000 UTC 3/14	Southern Plains	—	1.00 in.	Null
48	2021	3	12	0730 UTC 3/12	1200 UTC 3/12	Central Plains	M99 kt	1.00 in.	Sig. Dam.
49	2021	3	11	0000 UTC 3/11	0400 UTC 3/11	Great Lakes	—	—	Pot. Dam.
50	2021	2	26	2300 UTC 2/25	1200 UTC 2/26	Gulf Coast	—	2.00 in.	Null
51	2021	2	6	1700 UTC 2/6	2100 UTC 2/6	Gulf Coast	—	—	Null
52	2021	1	25	0000 UTC 1/25	1000 UTC 1/25	Southern Plains	E75 kt	1.25 in.	Sig. Dam.
53*	2020	6	8–9	0000 UTC 6/7	0100 UTC 6/10	Northern Plains	M99 kt	2.00 in.	Sig. Dam.
54*	2020	5	3–4	0300 UTC 5/4	2100 UTC 5/4	Central Plains	E96 kt	2.75 in.	Sig. Dam.
55*	2018	4	13	0800 UTC 4/13	1700 UTC 4/13	Great Lakes	E72 kt	1.75 in.	Sig. Dam.
56*	2017	4	10–11	1000 UTC 4/9	0900 UTC 4/10	Great Lakes	E83 kt	1.00 in.	Sig. Dam.
57*	2014	4	12	1200 UTC 4/12	0100 UTC 4/13	Great Lakes	E75 kt	1.00 in.	Sig. Dam.
58*	2010	5	6–7	0000 UTC 5/7	1200 UTC 5/7	Mississippi River valley	E70 kt	2.75 in.	Sig. Dam.
59*	1997	6	20	0300 UTC 6/20	1030 UTC 6/20	Northern Plains	E78 kt	2.75 in.	Sig. Dam.
60*	1996	4	20	2100 UTC 4/19	0600 UTC 4/20	Great Lakes	E90 kt	1.75 in.	Sig. Dam.

Brought to you by NOAA Central Library | Unauthenticated | Downloaded 08/28/24 03:27 PM UTC

REFERENCES

Anderson, E. J., and G. E. Mann, 2020: A high-amplitude atmospheric inertia–gravity wave-induced meteotsunami in Lake Michigan. *Nat. Hazards*, **106**, 1489–1501, https://doi.org/10.1007/s11069-020-04195-2.

Ashley, W. S., and T. L. Mote, 2005: Derecho hazards in the United States. *Bull. Amer. Meteor. Soc.*, **86**, 1577–1592, https://doi.org/10.1175/BAMS-86-11-1577.

Atkins, N. T., and M. St. Laurent, 2009: Bow echo mesovortices. Part I: Processes that influence their damaging potential. *Mon. Wea. Rev.*, **137**, 1497–1513, https://doi.org/10.1175/2008MWR2649.1.

——, C. S. Bouchard, R. W. Przybylinski, R. J. Trapp, and G. Schmocker, 2005: Damaging surface wind mechanisms within the 10 June 2003 Saint Louis bow echo during BAMEX. *Mon. Wea. Rev.*, **133**, 2275–2296, https://doi.org/10.1175/MWR2973.1.

Bernardet, L. R., and W. R. Cotton, 1998: Multiscale evolution of a derecho-producing mesoscale convective system. *Mon. Wea. Rev.*, **126**, 2991–3015, https://doi.org/10.1175/1520-0493(1998)126<2991:MEOADP>2.0.CO;2.

Bernstein, B. C., and R. H. Johnson, 1994: A dual-Doppler radar study of an OK PRE-STORM heat burst event. *Mon. Wea. Rev.*, **122**, 259–273, https://doi.org/10.1175/1520-0493(1994)122<0259:ADDRSO>2.0.CO;2.

Blake, B. T., D. B. Parsons, K. R. Haghi, and S. G. Castleberry, 2017: The structure, evolution, and dynamics of a nocturnal convective system simulated using the WRF-ARW model. *Mon. Wea. Rev.*, **145**, 3719–3201, https://doi.org/10.1175/MWR-D-16-0360.1.

Boettcher, J. B., and E. S. Bentley, 2022: WSR-88D sidelobe contamination: From a conceptual model to diagnostic strategies for improving NWS warning performance. *Wea. Forecasting*, **37**, 853–869, https://doi.org/10.1175/WAF-D-21-0155.1.

Chen, F., and J. Dudhia, 2001: Coupling an advanced land surface–hydrology model with the Penn State–NCAR MM5 modeling system. Part I: Model implementation and sensitivity. *Mon. Wea. Rev.*, **129**, 569–585, https://doi.org/10.1175/1520-0493(2001)129<0569:CAALSH>2.0.CO;2.

Childs, S. J., R. S. Schumacher, and R. D. Adams-Selin, 2021: High-resolution observations of a destructive macroburst. *Mon. Wea. Rev.*, **149**, 2875–2896, https://doi.org/10.1175/MWR-D-20-0412.1.

Christie, D. R., K. J. Murihead, and A. L. Hales, 1978: On solitary waves in the atmosphere. *J. Atmos. Sci.*, **35**, 805–825, https://doi.org/10.1175/1520-0469(1978)035<0805:OSWITA>2.0.CO;2.

Clarke, R. H., R. K. Smith, and D. G. Reid, 1981: The morning glory of the Gulf of Carpentaria: An atmospheric undular bore. *Mon. Wea. Rev.*, **109**, 1726–1750, https://doi.org/10.1175/1520-0493(1981)109<1726:TMGOTG>2.0.CO;2.

Coleman, T. A., and K. R. Knupp, 2009: Factors affecting surface wind speeds in gravity waves and wake lows. *Wea. Forecasting*, **24**, 1664–1679, https://doi.org/10.1175/2009WAF2222248.1.

Colman, B. R., 1990: Thunderstorms above frontal surfaces in environments without positive CAPE. Part I: A climatology. *Mon. Wea. Rev.*, **118**, 1103–1122, https://doi.org/10.1175/1520-0493(1990)118<1103:TAFSIE>2.0.CO;2.

Doviak, R. J., and R. Ge, 1984: An atmospheric solitary gust observed with a Doppler radar, a tall tower and a surface network. *J. Atmos. Sci.*, **41**, 2259–2573, https://doi.org/10.1175/1520-0469(1984)041<2559:AASGOW>2.0.CO;2.

Dowell, D. C., and Coauthors, 2022: The High-Resolution Rapid Refresh (HRRR): An hourly updating convection-allowing forecast model. Part I: Motivation and system description. *Wea. Forecasting*, **37**, 1371–1395, https://doi.org/10.1175/WAF-D-21-0151.1.

Du, Y., and F. Zhang, 2019: Banded convective activity associated with mesoscale gravity waves over southern China. *J. Geophys. Res. Atmos.*, **124**, 1912–1930, https://doi.org/10.1029/2018JD029523.

Edwards, R., J. T. Allen, and G. W. Carbin, 2018: Reliability and climatological impacts of convective wind estimations. *J. Appl. Meteor. Climatol.*, **57**, 1825–1845, https://doi.org/10.1175/JAMC-D-17-0306.1.

Fovell, R. G., G. L. Mullendore, and S.-H. Kim, 2006: Discrete propagation in numerically simulated nocturnal squall lines. *Mon. Wea. Rev.*, **134**, 3735–3752, https://doi.org/10.1175/MWR3268.1.

French, A. J., and M. D. Parker, 2010: The response of simulated nocturnal convective systems to a developing low-level jet. *J. Atmos. Sci.*, **67**, 3384–3408, https://doi.org/10.1175/2010JAS3329.1.

Fujita, T. T., 1981: Tornadoes and downbursts in the context of generalized planetary scales. *J. Atmos. Sci.*, **38**, 1511–1534, https://doi.org/10.1175/1520-0469(1981)038<1511:TADITC>2.0.CO;2.

Fulton, R., D. S. Zrnić, and R. J. Doviak, 1990: Initiation of a solitary wave family in the demise of a nocturnal thunderstorm density current. *J. Atmos. Sci.*, **47**, 319–337, https://doi.org/10.1175/1520-0469(1990)047<0319:IOASWF>2.0.CO;2.

Haertel, P. T., R. H. Johnson, and S. N. Tulich, 2001: Some simple simulations of thunderstorm outflows. *J. Atmos. Sci.*, **58**, 504–516, https://doi.org/10.1175/1520-0469(2001)058<0504:SSSOTO>2.0.CO;2.

Hales, J. E., Jr., 1988: Improving the watch/warning program through use of significant event data. Preprints, *15th Conf. on Severe Local Storms*, Baltimore, MD, Amer. Meteor. Soc., 165–168.

Horgan, K. L., D. M. Schultz, J. E. Hales Jr., S. F. Corfidi, and R. H. Johns, 2007: A five-year climatology of elevated severe convective storms in the United States east of the Rocky Mountains. *Wea. Forecasting*, **22**, 1031–1044, https://doi.org/10.1175/WAF1032.1.

Iacono, M. J., J. S. Delamere, E. J. Mlawer, M. W. Shephard, S. A. Clough, and W. D. Collins, 2008: Radiative forcing by long-lived greenhouse gases: Calculations with the AER radiative transfer models. *J. Geophys. Res.*, **113**, D12103, https://doi.org/10.1029/2008JD009944.

Ibrahim, I., G. A. Kopp, and D. M. L. Sills, 2023: Retrieval of peak thunderstorm wind velocities using WSR-88D weather radars. *J. Atmos. Oceanic Technol.*, **40**, 237–251, https://doi.org/10.1175/JTECH-D-22-0028.1.

Janjić, Z. I., 2001: Nonsingular implementation of the Mellor-Yamada level 2.5 scheme in the NCEP Meso Model. NCEP Office Note 437, 61 pp.

Kelly, D. L., J. T. Schaefer, and C. A. Doswell III, 1985: Climatology of nontornadic severe thunderstorm events in the United States. *Mon. Wea. Rev.*, **113**, 1997–2014, https://doi.org/10.1175/1520-0493(1985)113<1997:CONSTE>2.0.CO;2.

Knupp, K. R., 1996: Structure and evolution of a long-lived, microburst-producing storm. *Mon. Wea. Rev.*, **124**, 2785–2806, https://doi.org/10.1175/1520-0493(1996)124<2785:SAEOAL>2.0.CO;2.

——, 2006: Observational analysis of a gust front to bore to solitary wave transition within an evolving nocturnal boundary

Brought to you by NOAA Central Library | Unauthenticated | Downloaded 08/28/24 03:27 PM UTC

layer. *J. Atmos. Sci.*, **63**, 2016–2035, https://doi.org/10.1175/JAS3731.1.

Koch, S. E., and W. L. Clark, 1999: A nonclassical cold front observed during COPS-91: Frontal structure and the process of severe storm initiation. *J. Atmos. Sci.*, **56**, 2862–2890, https://doi.org/10.1175/1520-0469(1999)056<2862:ANCFOD>2.0.CO;2.

——, and S. Saleeby, 2001: An automated system for the analysis of gravity waves and other mesoscale phenomena. *Wea. Forecasting*, **16**, 661–679, https://doi.org/10.1175/1520-0434(2001)016<0661:AASFTA>2.0.CO;2.

——, R. E. Golus, and P. B. Dorian, 1988: A mesoscale gravity wave event observed during CCOPE. Part II: Interactions between mesoscale convective systems and the antecedent waves. *Mon. Wea. Rev.*, **116**, 2545–2569, https://doi.org/10.1175/1520-0493(1988)116<2545:AMGWEO>2.0.CO;2.

——, W. Feltz, F. Fabry, M. Pagowski, B. Geerts, K. M. Bedka, D. O. Miller, and J. W. Wilson, 2008: Turbulent mixing processes in atmospheric bores and solitary waves deduced from profiling systems and numerical simulation. *Mon. Wea. Rev.*, **136**, 1373–1400, https://doi.org/10.1175/2007MWR2252.1.

Koppel, L. L., L. F. Bosart, and D. Keyser, 2000: A 25-yr climatology of large-amplitude hourly surface pressure changes over the conterminous United States. *Mon. Wea. Rev.*, **128**, 51–68, https://doi.org/10.1175/1520-0493(2000)128<0051:AYCOLA>2.0.CO;2.

Kuchera, E. L., and M. D. Parker, 2006: Severe convective wind environments. *Wea. Forecasting*, **21**, 595–612, https://doi.org/10.1175/WAF931.1.

MacIntosh, C. W., and M. D. Parker, 2017: The 6 May 2010 elevated supercell during VORTEX2. *Mon. Wea. Rev.*, **145**, 2635–2657, https://doi.org/10.1175/MWR-D-16-0329.1.

Mahapatra, P. R., R. J. Doviak, and D. S. Zrnić, 1991: Multisensor observation of an atmospheric undular bore. *Bull. Amer. Meteor. Soc.*, **72**, 1468–1480, https://doi.org/10.1175/1520-0477(1991)072<1468:MOOAAU>2.0.CO;2.

Marsham, J. H., K. A. Browning, J. C. Nicol, D. J. Parker, E. G. Norton, A. M. Blyth, U. Corsmeier, and F. M. Perry, 2010: Multi-sensor observations of a wave beneath an impacting rear-inflow jet in an elevated mesoscale convective system. *Quart. J. Roy. Meteor. Soc.*, **136**, 1788–1812, https://doi.org/10.1002/qj.669.

——, S. B. Trier, T. M. Weckwerth, and J. W. Wilson, 2011: Observations of elevated convection initiation leading to a surface-based squall line during 13 June IHOP_2002. *Mon. Wea. Rev.*, **139**, 247–271, https://doi.org/10.1175/2010MWR3422.1.

Mellor, G. L., and T. Yamada, 1982: Development of a turbulence closure model for geophysical fluid problems. *Rev. Geophys.*, **20**, 851–875, https://doi.org/10.1029/RG020i004p00851.

Parker, M. D., 2008: Response of simulated squall lines to low-level cooling. *J. Atmos. Sci.*, **65**, 1323–1341, https://doi.org/10.1175/2007JAS2507.1.

Parsons, D. B., K. R. Haghi, K. T. Halbert, B. Elmer, and J. Wang, 2019: The potential role of atmospheric bores and gravity waves in the initiation and maintenance of nocturnal convection over the southern Great Plains. *J. Atmos. Sci.*, **76**, 43–68, https://doi.org/10.1175/JAS-D-17-0172.1.

Peltier, W. R., and T. L. Clark, 1979: The evolution and stability of finite-amplitude mountain waves. Part II: Surface wave drag and severe downslope windstorms. *J. Atmos. Sci.*, **36**, 1498–1529, https://doi.org/10.1175/1520-0469(1979)036<1498:TEASOF>2.0.CO;2.

Powers, J. G., and R. J. Reed, 1993: Numerical simulation of the large-amplitude mesoscale gravity-wave event of 15 December 1987 in the central United States. *Mon. Wea. Rev.*, **121**, 2285–2308, https://doi.org/10.1175/1520-0493(1993)121<2285:NSOTLA>2.0.CO;2.

——, and Coauthors, 2017: The Weather Research and Forecasting Model: Overview, system efforts, and future directions. *Bull. Amer. Meteor. Soc.*, **98**, 1717–1737, https://doi.org/10.1175/BAMS-D-15-00308.1.

Proctor, F. H., 1989: Numerical simulations of an isolated microburst. Part II: Sensitivity experiments. *J. Atmos. Sci.*, **46**, 2143–2165, https://doi.org/10.1175/1520-0469(1989)046<2143:NSOAIM>2.0.CO;2.

Przybylinski, R. W., 1995: The bow echo: Observations, numerical simulations, and severe weather detection methods. *Wea. Forecasting*, **10**, 203–218, https://doi.org/10.1175/1520-0434(1995)010<0203:TBEONS>2.0.CO;2.

Reif, D. W., and H. B. Bluestein, 2017: A 20-year climatology of nocturnal convection initiation over the central and southern Great Plains during the warm season. *Mon. Wea. Rev.*, **145**, 1615–1639, https://doi.org/10.1175/MWR-D-16-0340.1.

Rottman, J. W., F. Einaudi, S. E. Koch, and W. L. Clark, 1992: A case study of penetrative convection and gravity waves over the PROFS mesonetwork on 23 July 1983. *Meteor. Atmos. Phys.*, **47**, 205–227, https://doi.org/10.1007/BF01025618.

Ruppert, J. H., Jr., and L. F. Bosart, 2014: A case study of the interaction of a mesoscale gravity wave with a mesoscale convective system. *Mon. Wea. Rev.*, **142**, 1403–1429, https://doi.org/10.1175/MWR-D-13-00274.1.

——, S. E. Koch, X. Chen, Y. Du, A. Seimon, Y. Q. Sun, J. Wei, and L. F. Bosart, 2022: Mesoscale gravity waves and midlatitude weather: A tribute to Fuqing Zhang. *Bull. Amer. Meteor. Soc.*, **103**, E129–E156, https://doi.org/10.1175/BAMS-D-20-0005.1.

Schmidt, J. M., and W. R. Cotton, 1989: A high plains squall line associated with severe surface winds. *J. Atmos. Sci.*, **46**, 281–302, https://doi.org/10.1175/1520-0469(1989)046<0281:AHPSLA>2.0.CO;2.

Schmocker, G. K., R. W. Przybylinski, and Y. J. Lin, 1996: Forecasting the initial onset of damaging downburst winds associated with a mesoscale convective system (MCS) using the midaltitude radial convergence (MARC) signature. Preprints, *15th Conf. on Weather Analysis and Forecasting*, Norfolk, VA, Amer. Meteor. Soc., 306–311.

Schumacher, R. S., S. J. Childs, and R. D. Adams-Selin, 2023: Intense surface winds from gravity wave breaking in simulations of a destructive macroburst. *Mon. Wea. Rev.*, **151**, 775–793, https://doi.org/10.1175/MWR-D-22-0103.1.

Sherburn, K. D., M. J. Bunkers, and A. J. Mose, 2021: Radar-based comparison of thunderstorm outflow boundary speeds versus peak wind gusts from automated stations. *Wea. Forecasting*, **36**, 1387–1403, https://doi.org/10.1175/WAF-D-20-0221.1.

Smith, B. T., T. E. Castellanos, A. C. Winters, C. M. Mead, A. R. Dean, and R. L. Thompson, 2013: Measured severe convective wind climatology and associated convective modes of thunderstorms in the contiguous United States, 2003–09. *Wea. Forecasting*, **28**, 229–236, https://doi.org/10.1175/WAF-D-12-00096.1.

Smull, B. F., and R. A. Houze Jr., 1987: Rear inflow in squall lines with trailing stratiform precipitation. *Mon. Wea. Rev.*, **115**, 2869–2889, https://doi.org/10.1175/1520-0493(1987)115<2869:RIISLW>2.0.CO;2.

Brought to you by NOAA Central Library | Unauthenticated | Downloaded 08/28/24 03:27 PM UTC

Tepper, M., 1950: A proposed mechanism of squall lines: The pressure jump line. *J. Meteor.*, **7**, 21–29, https://doi.org/10.1175/1520-0469(1950)007<0021:APMOSL>2.0.CO;2.

Thompson, G., P. R. Field, R. M. Rasmussen, and W. D. Hall, 2008: Explicit forecasts of winter precipitation using an improved bulk microphysics scheme. Part II: Implementable of a new snow parameterization. *Mon. Wea. Rev.*, **136**, 5095–5115, https://doi.org/10.1175/2008MWR2387.1.

Toms, B. A., J. M. Tomaszewski, D. D. Turner, and S. E. Koch, 2017: Analysis of a lower-tropospheric gravity wave train using direct and remote sensing measurement systems. *Mon. Wea. Rev.*, **145**, 2791–2812, https://doi.org/10.1175/MWR-D-16-0216.1.

Trapp, R. J., D. M. Wheatley, N. T. Atkins, R. W. Przybylinski, and R. Wolf, 2006: Buyer beware: Some words of caution on the use of severe wind reports in postevent assessment and research. *Wea. Forecasting*, **21**, 408–415, https://doi.org/10.1175/WAF925.1.

Uccellini, L. W., 1975: A case study of apparent gravity wave initiation of severe convective storms. *Mon. Wea. Rev.*, **103**, 497–513, https://doi.org/10.1175/1520-0493(1975)103<0497:ACSOAG>2.0.CO;2.

——, and S. E. Koch, 1987: The synoptic setting and possible energy sources for mesoscale wave disturbances. *Mon. Wea. Rev.*, **115**, 721–729, https://doi.org/10.1175/1520-0493(1987)115<0721:TSSAPE>2.0.CO;2.

Wakimoto, 2001: Convectively driven high winds. *Severe Convective Storms*, *Meteor. Monogr.*, No. 50, Amer. Meteor. Soc., 255–298.

Wakimoto, R. M., H. V. Murphey, C. A. Davis, and N. T. Atkins, 2006: High winds generated by bow echoes. Part II: The relationship between the mesovortices and damaging straight-line winds. *Mon. Wea. Rev.*, **134**, 2813–2829, https://doi.org/10.1175/MWR3216.1.

Weisman, M. L., 1993: The genesis of severe, long-lived bow echoes. *J. Atmos. Sci.*, **50**, 645–670, https://doi.org/10.1175/1520-0469(1993)050<0645:TGOSLL>2.0.CO;2.

——, and R. J. Trapp, 2003: Low-level mesovortices within squall lines and bow echoes. Part I: Overview and dependence on environmental shear. *Mon. Wea. Rev.*, **131**, 2779–2803, https://doi.org/10.1175/1520-0493(2003)131<2779:LMWSLA>2.0.CO;2.

Zhang, F., and S. E. Koch, 2000: Numerical simulations of a gravity wave event over CCOPE. Part II: Waves generated by an orographic density current. *Mon. Wea. Rev.*, **128**, 2777–2796, https://doi.org/10.1175/1520-0493(2000)128<2777:NSOAGW>2.0.CO;2.

——, C. A. Davis, M. L. Kaplan, and S. E. Koch, 2001: Wavelet analysis and the governing dynamics of a large-amplitude mesoscale gravity-wave event along the East Coast of the United States. *Quart. J. Roy. Meteor. Soc.*, **127**, 2209–2245, https://doi.org/10.1002/qj.49712757702.

Brought to you by NOAA Central Library | Unauthenticated | Downloaded 08/28/24 03:27 PM UTC